Assessment of the Reconstructed Aerodynamics of the Mars Science Laboratory Entry Vehicle

Mark Schoenenberger,* John Van Norman,† Chris Karlgaard,‡ Prasad Kutty,§ and David Way¶
NASA Langley Research Center, Hampton, Virginia 23681

On 5 August 2012, the Mars Science Laboratory entry vehicle successfully entered the atmosphere of Mars, flying a guided entry until parachute deploy. The Curiosity rover landed safely in Gale crater upon completion of the entry, descent, and landing sequence. Preflight aerodynamic predictions are compared with the aerodynamic performance of the entry capsule identified from onboard flight data, including inertial-measurement-unit accelerometer and rate gyro information, and heat shield surface pressure measurements. From the onboard data, static force and moment coefficients have been extracted. These data are compared with the preflight aerodynamic database. The Mars Science Laboratory flight data represent the most complete and self-consistent record of a blunt capsule entering Mars collected to date. These data enable the separation of aerodynamic performance from atmospheric conditions. The comparisons show the Mars Science Laboratory aerodynamic characteristics have been successfully identified and resolved to an accuracy better than the aerodynamic database uncertainties used in preflight simulations. A number of small anomalies have been identified and are discussed. These data will help improve aerodynamic databases for future missions and will guide computational fluid dynamics development to improve predictions.

Nomenclature

A, B, C, D	=	frequency constants
a_x, a_y, a_z	=	acceleration components, m/s^2
C_A	=	axial force coefficient
$C_{A_{\text{Disp}}}$	=	dispersed axial force coefficient
C_D, C_L	=	drag and lift coefficients
C_l, C_m	=	roll and pitch moment coefficients
C_{m_α}	=	pitch moment slope, rad^{-1}
C_N	=	normal force coefficient
$C_{N_{\text{Disp}}}$	=	dispersed normal force coefficient
C_n	=	yaw moment coefficient
C_{n_β}	=	yaw moment slope, rad^{-1}
C_p	=	pressure coefficient
C_X	=	general force coefficient
C_x	=	general moment coefficient
C_Y	=	side force coefficient
d_{ref}	=	reference diameter, m
F_X	=	general aerodynamic force, N
f_y, f_z	=	oscillation frequencies, Hz
$\boldsymbol{I}$	=	moment-of-inertia tensor, kg · m^2
I_{yy}, I_{zz}	=	moment of inertia about aeroaxes, kg · m^2
$\boldsymbol{M}_{\text{Aero}}$	=	aerodynamic moment vector, N · m
$M_{\text{aero},i-j}$	=	aeromoment components, N · m
M_x	=	general aerodynamic moment, N · m
M_∞	=	freestream Mach number
m_{EV}	=	entry vehicle mass, kg
P_{1-7}	=	Mars entry atmospheric data system pressure ports
p, q, r	=	body rates, deg /s
p_i	=	measured pressure, Pa
p_∞	=	freestream static pressure, Pa
q_∞	=	freestream dynamic pressure, Pa
$q_{\infty,\text{MEADS}}$	=	Mars entry atmospheric data-system-derived q_∞, Pa
S_{ref}	=	reference area, m^2
t	=	time, s
$U_{C_x}^A$	=	database adder dispersion for C_x
$U_{C_x}^M$	=	database multiplier dispersion for C_x
V_∞	=	freestream velocity, m/s
v_x, v_y, v_z	=	freestream velocity components, m/s
x_{ac}, y_{ac}, z_{ac}	=	aerodynamic coordinate axes, m
$(x_{\text{c.g.}}, y_{\text{c.g.}}, z_{\text{c.g.}})/d$	=	normalized center of gravity position
$x_{\text{nose}}, y_{\text{nose}}, z_{\text{nose}}$	=	vehicle nose location, m
α	=	angle of attack, deg
α_{Total}	=	total angle of attack, deg
α_{Trim}	=	trim angle of attack, deg
β	=	angle of sideslip, deg
$\dot{\beta}$	=	sideslip rate of change, deg /s
ϕ_y, ϕ_z	=	frequency curve fit phase angles, deg
$\boldsymbol{\omega}$	=	angular rate vector, deg /s
$\dot{\boldsymbol{\omega}}$	=	angular acceleration vector, deg /s^2
ω_y, ω_z	=	angular rate components, deg /s

I. Introduction

ON 5 AUGUST 2012, the Mars Science Laboratory (MSL) entry vehicle (EV) successfully entered the Mars atmosphere and landed the Curiosity rover safely on its surface. Data collected from onboard instrumentation were used to reconstruct the entry trajectory and measure properties of the atmosphere traversed during deceleration to parachute deployment. The Mars entry atmospheric data system (MEADS) experiment flew aboard the MSL EV. Part of the Mars entry descent and landing instrumentation project (MEDLI), the MEADS experiment measured pressures at seven locations on the MSL heat shield. These pressure data were used to extract dynamic pressure, angle of attack, and angle of sideslip and help estimate Mach number. MSL carried an inertial measurement unit (IMU) that was used for navigation as the EV flew a guided entry to landing. Postflight, the IMU measurements of accelerations and rates were used to reconstruct the capsule's inertial velocity, position, and attitude history. The MSL aerodynamic database (ADB) was also compared against IMU accelerometer measurements to provide a semi-independent assessment of the wind-relative attitude during

entry. The different data products have been used to reconstruct the MSL trajectory individually, then combined into a reconstruction with an extended Kalman filtering approach. Previous recent missions to Mars [1–3] did not have surface pressure instrumentation on the entry vehicle forebody and could only measure the net forces and moments acting on the vehicle. Therefore, recent missions before MSL could not extract the aerodynamic coefficients without an assumption of the atmosphere properties or vice versa. Stagnation pressure measurements, with a reconstructed Mach number, provide an accurate estimate of freestream dynamic pressure. Therefore, capsule shape and atmosphere contributions can be separated with the full MSL entry data. The Viking entry vehicles [4] did have forebody pressure measurements during entry and a flight data set much like that of MSL; the atmosphere profile was reconstructed and an assessment of the aerodynamic performance was performed. The reconstruction methodologies used for MSL trace their roots back to Viking. Although a great deal of information was extracted and all subsequent Mars entries have relied on Viking heritage data (both preflight models and reconstructed data), the pressure-based attitude reconstructions of the Viking entries differed significantly from inertial reconstructions and a complete and self-consistent reconstruction was not fully realized [5,6].

This paper will provide an overview of the preflight MSL aerodynamic database and compare it with the aerodynamic performance reconstructed from flight data. The dynamic pressure history measured during entry is used to extract static force and moment coefficients. The preflight aerodynamic predictions used for mission design and flight operations simulations are compared with the reconstructed aerodynamic coefficients. Assessments of notable differences and general agreement between predicted and reconstructed static forces and moments are presented along with qualitative assessments of reaction control system (RCS) performance and capsule dynamic stability. The aerodynamic database uncertainty model is described and best-fit uncertainties on the reconstructed coefficients are estimated to help assess the accuracy of preflight predictions. The local pressure measurements observed by MEADS are compared with computational predictions and the net forces and moments predicted by those solutions. The differences between the MEADS-converged attitude and forces and moments, and the corresponding aerodynamic forces and moments predicted by the MSL aerodynamic database are compared and discussed.

To decelerate from entry velocity to parachute deploy conditions, the MSL mission used a blunt-body entry capsule. The Mars Science Laboratory EV was composed of a 70 deg sphere-cone heat shield and a backshell consisting of a stack of three truncated cones. The forebody shape is based on the heat shield geometry developed for the Viking Mars landers [7]. The backshell configuration is also similar to Viking, with a third truncated cone segment added to accommodate the parachute volume. The design capsule diameter was 4.519 m; it is the largest entry vehicle ever flown at Mars. During most of the entry, the capsule used a radial c.g. offset to fly at an angle of attack (approximately −16 deg at hypersonic conditions). This attitude produced lift to fly a guided entry profile, reducing the landing footprint to a size much smaller than any previous Mars mission. To fly the guided entry, the MSL EV carried four pairs of 68 lbf (nominal) (302.5 N) RCS jets to perform maneuvers and damp rates. The four pairs of jets could be fired rapidly in different combinations to provide control torques about roll, pitch, yaw, or any other axis by modulating the pulses of the jet.

A simplified drawing of the MSL capsule geometry representative of the flight vehicle and the grids used to populate the aerodynamic database with computational fluid dynamics (CFD) solutions is shown in Fig. 1. The aerodynamic database CFD calculations were run on grids based on geometry models developed for earlier versions of the heat shield. The flight capsule shoulder radius was increased slightly from early configurations and the maximum diameter was increased by about 19 mm due to an increase in heat shield thickness during the vehicle development process. The measured diameter of the as-built heat shield was 4.520 m. CFD studies were conducted to assess aerodynamic sensitivities to these shape changes and all were found to be well within the aerodynamic database uncertainties. The
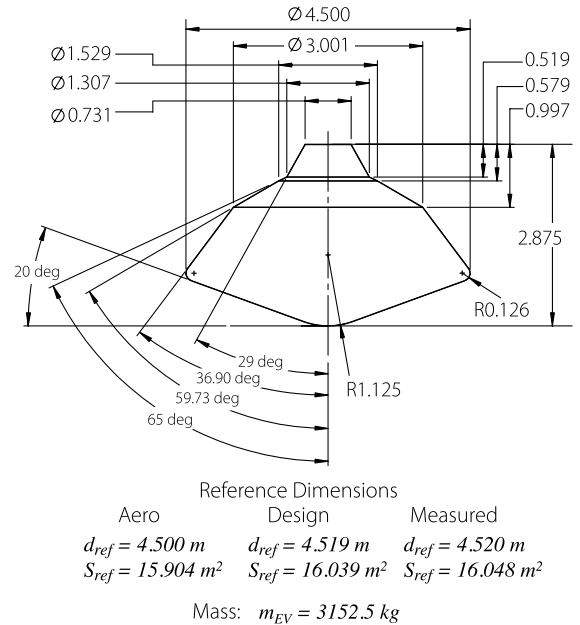

Fig. 1 Mars Science Laboratory entry vehicle representative dimensions (meters).

simplified geometry in Fig. 1 is a description of the geometry used for aerodynamic modeling. Three sets of reference dimensions are given. The nominal or "Aero" values are those carried during MSL development and represent the original heat shield dimensions used for aerodynamic database grid generation. The second set contains the design dimensions of the flight article and the third lists the measured values of the as-built vehicle. The aerodynamic coefficients presented and discussed in this paper are consistent with the design values listed in Fig. 1. The differences between the design and measured reference values are negligible for reconstruction purposes.

The aerodynamic force and moment definitions, and the design and measured c.g. locations in the aerodynamic coordinate frame are shown in Fig. 2. The coordinate system origin is located at the capsule nose. The aerodynamic coordinates are the standard convention for defining aircraft coefficients aligned to the capsule body (C_A, C_N), rather than the velocity vector (C_L, C_D). The aerodynamic coefficients shown in Fig. 2 are defined as

Forces:

$$C_X = \frac{F_X}{q_\infty S_{\text{ref}}} \tag{1}$$

Moments:

$$C_x = \frac{M_x}{q_\infty S_{\text{ref}} d_{\text{ref}}} \tag{2}$$

where F_X and M_x are the aerodynamic forces and moments acting on the capsule, q_∞ is the freestream dynamic pressure based on the freestream density and wind-relative freestream velocity ($q_\infty = \frac{1}{2}\rho_\infty V_\infty^2$) and S_{ref} and d_{ref} are the measured reference area and diameter of the MSL EV, respectively.

This assessment focused on comparing the reconstructed aerodynamic performance of the MSL EV to preflight predictions. The vehicle passed through many additional phases of flight after the aeroshell served its function of slowing the payload from approximately 5845 m/s to a safe parachute deploy condition near Mach 1.7. Just before parachute deploy (near Mach 2.0), a series of six balance masses were jettisoned to eliminate the radial c.g. offset, trimming the capsule to a near-zero angle of attack for safe parachute deployment. During this mass jettison, the vehicle was also banked 180 deg from its entry attitude to place the landing radar in an attitude more favorable for acquiring the ground. The jettison of balance masses and the bank maneuver are collectively (and colloquially) referred to as the "straighten up and fly right" (SUFR) maneuver. The initiation
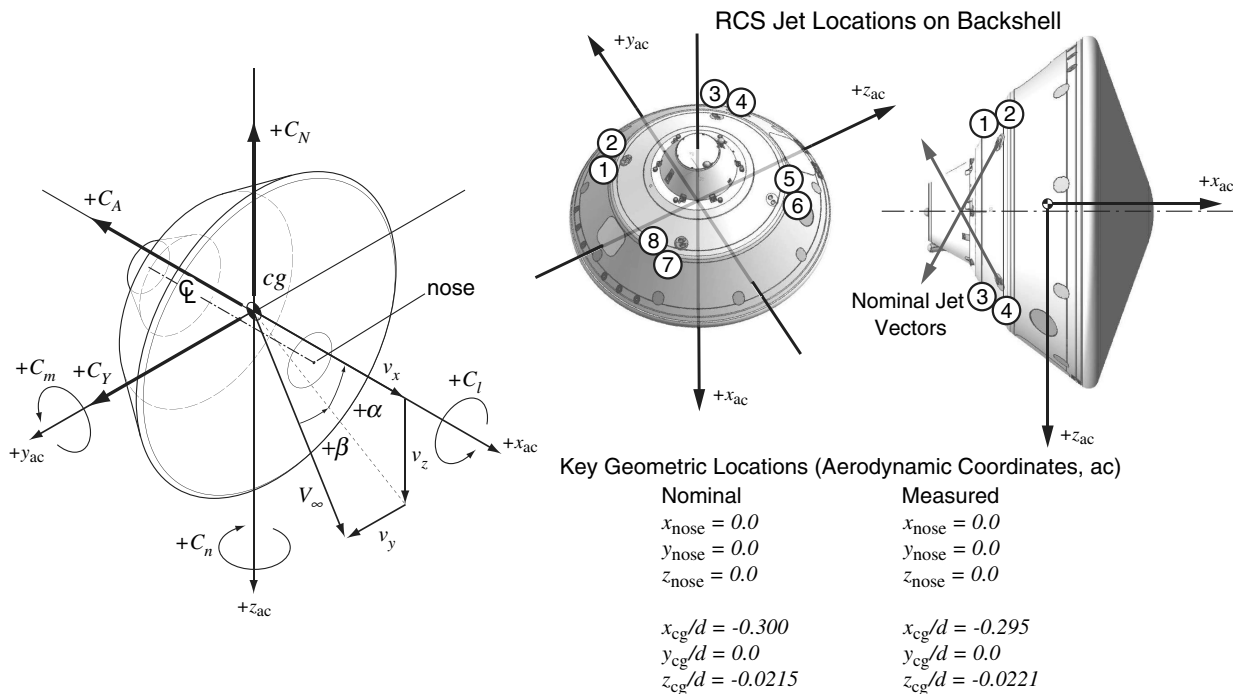
RCS Jet Locations on Backshell

Nominal Jet Vectors

Key Geometric Locations (Aerodynamic Coordinates, ac)

Nominal	Measured
$x_{nose} = 0.0$	$x_{nose} = 0.0$
$y_{nose} = 0.0$	$y_{nose} = 0.0$
$z_{nose} = 0.0$	$z_{nose} = 0.0$
$x_{cg}/d = -0.300$	$x_{cg}/d = -0.295$
$y_{cg}/d = 0.0$	$y_{cg}/d = 0.0$
$z_{cg}/d = -0.0215$	$z_{cg}/d = -0.0221$

Fig. 2 MSL aerodynamic and coordinate frame definitions.

of this maneuver (marked by the first balance mass jettison) will be noted in plots within this paper as the RCS firing and mass jettisons introduce vibrations and accelerations that influenced IMU and pressure measurements.

After parachute deploy, the vehicle decelerated to a safe velocity for the MSL rover, with its propulsive descent stage (DS), to drop from the backshell and enter a powered flight mode. Using eight throttleable descent engines to provide deceleration and full six-degree-of-freedom (6DOF) control, the powered descent vehicle (rover plus DS) then diverted from the flight path of the parachute-backshell system to avoid recontact and proceeded to descend to just above the Mars surface where the rover was lowered on tethers to a safe landing in a maneuver called the "sky crane." In general, MSL flew well through all phases of entry, descent, and landing. The assessment of flight performance during phases after parachute deploy are documented elsewhere [8] and will not be discussed further here.

A trajectory representative of the MSL flight profile, generated by preflight simulation, is shown in Fig. 3 compared with the trajectory simulation from which the MSL conditions were taken for aerodynamic database CFD computations (MSL 05-22). The Mars exploration rover (MER) design trajectory is shown for reference as
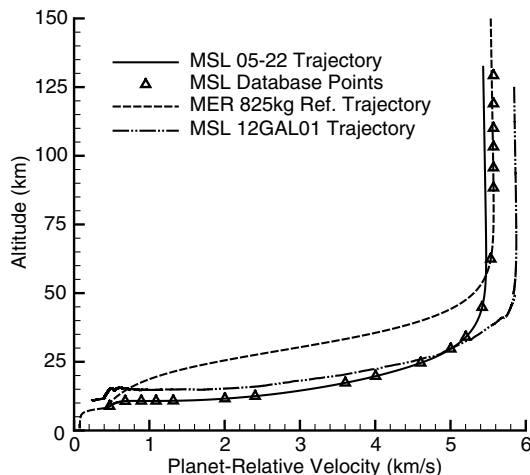
well. These trajectories help visualize the path that the MSL capsule took during its descent and deceleration through the Martian atmosphere. The MSL capsule flew deeper into the atmosphere earlier as compared with the nonlifting MER trajectory. In addition to slowing the vehicle, MSL flew a guided entry, using lift to minimize downrange error and later correct heading errors to fly to a small landing footprint. Flying deeper in the atmosphere provided greater dynamic pressure for more lift force to improve guided flight performance. The MSL vehicle lofted higher than the reference trajectory used for CFD conditions. Comparison of computations along both trajectories shows that any errors due to CFD cases being run at conditions away from the actual flight profile were small. The potential sources of error include trajectory conditions, turbulence models, gas models used in CFD codes, and others. Engineering-judgment interpretations of observed differences, based on preflight error analysis, will be provided here. Conclusively identifying the specific error sources that reconcile differences is beyond the scope of this work.

The LAURA [9] CFD code was used to predict the static aerodynamic force and moment coefficients in the continuum flight regime. These data were used to design the MSL entry trajectory and, during flight operations, to target the final landing location. LAURA is a finite volume shock-capturing algorithm capable of calculating flows in chemical and thermal nonequilibrium. LAURA can be used for inviscid thin-layer Navier–Stokes or full Navier–Stokes computations. The solutions in the MSL aerodynamic database were run laminar with nonblowing wall boundary conditions. and solved the thin-layer Navier Stokes equations. The calculations were performed on Intel Linux clusters (32 bit word length) with LAURA version "LAURA_intel" (last modified 17 March 2006). The calculations for a given solution were spread over many processors via Message Passing Interface [10].

The LAURA CFD matrix is shown in Fig. 4. The conditions along the reference trajectory, shown in Fig. 3, were used as freestream conditions for the flight CFD calculations. More details of the MSL aerodynamic database are described in papers by Schoenenberger et al. [11] and Dyakonov et al. [12]. The aerodynamic coefficients presented in this paper for comparison to the reconstructed aerodynamic coefficients were obtained using the same MSL aerodynamic database code as was used in preflight simulations (using reconstructed flight trajectory states). Note that CFD is used for all data points, but for all supersonic points noted in Fig. 4, the backshell

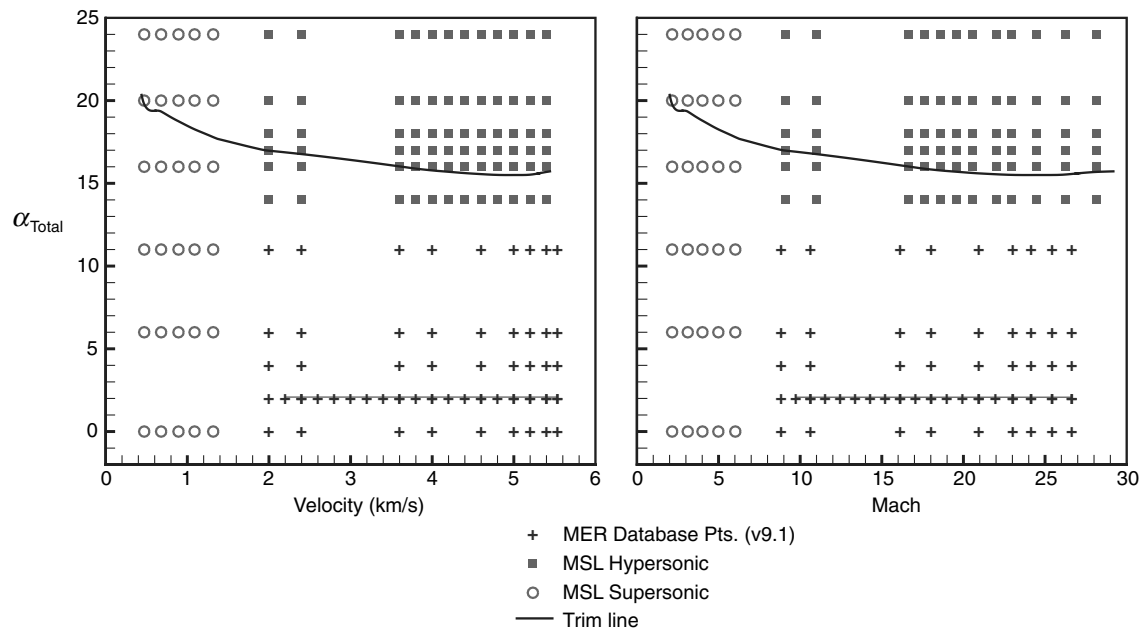**Fig. 3 MSL database points along design and reference trajectories.**

Fig. 4   CFD Matrix in MSL preflight database (predicted trim angle shown).

contribution is not accounted for using the CFD pressure distributions. Instead, the backshell contribution to axial force is modeled with a curve fit derived from Viking flight measurements of backshell pressure. The backshell contributions to normal and side force coefficients, as well as pitch and yaw moments, were found to be negligible. Therefore, C_A is the only coefficient with a correction. The base correction model is presented in the paper by Dyakonov et al. [12]. This methodology was developed for Mars Pathfinder and used again for the Mars exploration rover and Mars Phoenix aerodynamic databases. The MEADS data set is the first to provide any independent information to assess this base correction.

II.   Methods

To assess the preflight aerodynamic database and extract as much detail as possible, an accurate reconstruction of the MSL entry trajectory is required. The path the EV followed during entry, its orientation, and full knowledge of atmosphere properties, including wind velocity, are required to extract the aerodynamic coefficients. The reconstruction efforts sponsored by the MEDLI project have developed the methodologies to use onboard instrumentation including MEADS pressure measurements and the descent inertial measurement unit (DIMU) to reconstruct the MSL capsule entry as accurately as possible and to extract aerodynamic coefficients for comparison with preflight predictions. Karlgaard et al. [13–15] have developed the MSL reconstruction methodology based on techniques used for a number of recent flight projects, including Ares 1-X and Hyper-X/X-43-A. The reconstruction process and how the capsule state, aerodynamic performance, and Mars atmosphere were reconstructed from inertial and pressure telemetry is described briefly next, with details provided in cited papers. This section is intended to provide sufficient detail regarding the reconstruction process to understand the data being compared with preflight predictions.

A.   Instrumentation

Accurate reconstruction of the MSL entry was possible because of two key instruments. First, the DIMU provided a set of angular rates and axial accelerations to reconstruct the inertial path and attitude during entry. Second, the MEADS experiment provided seven pressure measurements on the heat shield that served as a flush air data system to measure the dynamic pressure that the capsule experienced during entry as well as the wind-relative angles of attack α and sideslip β.

The pressure port locations on the MSL heat shield and a drawing of an installed transducer are shown in Fig. 5. The port locations were

selected to measure stagnation pressure and resolve angles of attack and sideslip. Ports 1 and 2 were located at or near the expected stagnation point during entry to provide an accurate stagnation pressure with which to reconstruct freestream dynamic pressure. Ports 6 and 7 are located off of the nominal pitch plane to provide sideslip information. Ports 1–5 work together to resolve angle of attack. Although these groupings of port locations were selected to be sensitive to the noted variables, the solution algorithm uses all seven transducers together to solve for the angle of attack and sideslip simultaneously, matching measured pressures with a CFD model. The full-scale range of the transducers was 5.0 psi (34.474 kPa). This range was selected to ensure that no transducer overranged at peak dynamic pressure during entry, but still provided accurate dynamic pressure and attitude measurements down to 850 Pa (a MEADS design requirement). Pressure data were collected at 8.0 Hz through all of the entry until just before heat shield jettison. Details of the hardware, its installation, and calibration are summarized by Munk et al. [16].

The MSL heat shield was built with an aluminum honeycomb structure covered with a thermal protection system (TPS) consisting of phenolic impregnated carbon ablator (PICA) tiles. MSL was the first vehicle flown at Mars with a tiled heat shield. The tile arrangement and the cross section of the structure and TPS material are presented in Fig. 5. The gaps between tiles were filled with room-temperature vulcanizing (RTV) sealant. Port locations were selected in part to maintain "safe" distances from the gaps to avoid aerodynamic influences on pressure measurements from surface features associated with local ablation or roughness near the seams.

The DIMU, which was used to provide navigation information during entry, descent, and landing, was a Honeywell miniature inertial measurement unit.[**] The device measured angle and velocity increments across internal time steps, recording them at 200 Hz. These increments were converted to angular rates (then quaternions) and accelerations to perform an inertial reconstruction of the capsule trajectory. The DIMU was installed to an angular accuracy of 1 mrad about each axis relative to the descent stage. Through a stack up of quality assurance measurements it was determined that the orientation knowledge of the DIMU relative to the heat shield surface was also on the order of 1 mrad.

[**]Data available online at http://www51.honeywell.com/aero/common/documents/myaerospacecatalog-documents/MIMU.pdf [retrieved 28 May 2014].

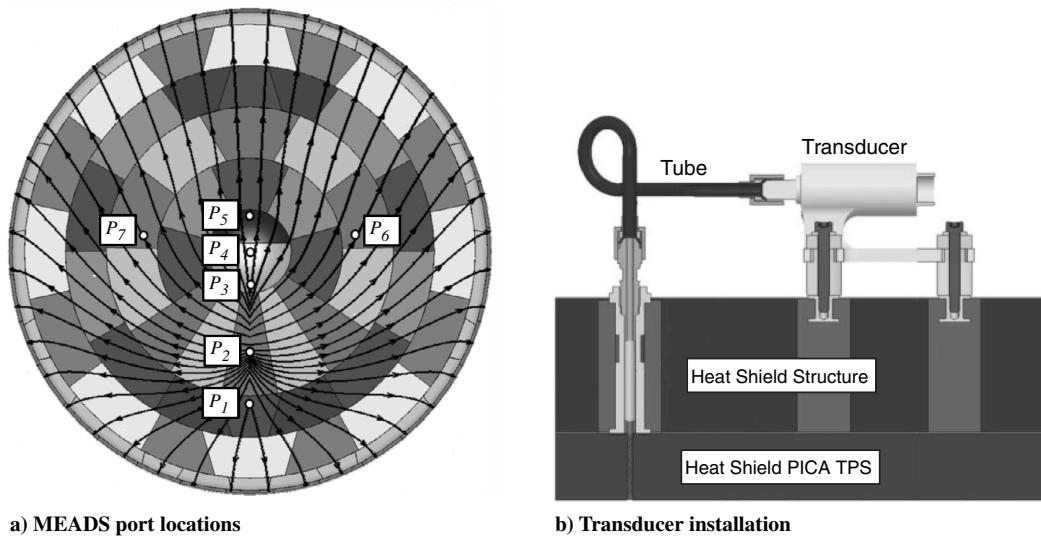a) MEADS port locations   b) Transducer installation

Fig. 5   MEADS layout and mechanical installation.

B.   Reconstruction of MSL Entry Trajectory

Papers by Karlgaard et al. [17–19] describe the preliminary reconstruction process and extended Kalman filter (EKF) reconstruction results using all available data sets. For this analysis, the DIMU and MEADS data were used together to determine the estimated entry trajectory of the MSL entry capsule. The aerodynamic model reconciliation described in Karlgaard et al. [19] uses two separate reconstruction methods to get an appreciation of the sensitivity of the extracted aerodynamic coefficients to the remaining unknowns in the reconstruction process (primarily winds and density). These techniques are semi-independent methods that use different portions of the entire data set. The first technique is a pure inertial solution and the second approach makes primary use of the MEADS pressure measurements aided by the magnitude of the capsule velocity along the entry trajectory.

The pure inertial reconstruction (referred to in this paper as the DIMU reconstruction) is based on a direct numerical integration of the measured accelerations and angular rates, using initial conditions obtained from orbit determination. An assumed atmosphere profile based on MSL-project mesoscale models was used to produce atmospheric-relative quantities, such as Mach number and dynamic pressure. The angles of attack and sideslip are calculated from the velocity components along the aerodynamic axes determined from the numerical integration of the DIMU accelerations and rates. The

atmosphere model assumed no local winds relative to the rotating planet.

The MEADS pressure reconstruction (referred to as the MEADS/ DIMU or simply MEADS reconstruction) uses a nonlinear least-squares algorithm to produce estimates of angle of attack, angle of sideslip, dynamic pressure, and static pressure. This least-squares algorithm includes a novel IMU-aiding approach in which the DIMU velocity magnitude is used to improve the estimate of Mach number. Atmospheric density is computed from the dynamic pressure estimate and the DIMU velocity, assuming no winds. The MEADS dynamic pressure and DIMU acceleration and angular rate measurements can also be combined to produce estimates of the vehicle aerodynamic forces and moments. It will be those reconstructed coefficients that are compared with preflight predictions later.

A comparison of the DIMU-reconstructed angles of attack and sideslip with a nominal entry simulation are plotted in Fig. 6. This Program to Optimize Simulated Trajectories II (POST2) [20] simulation, OD230, was initialized with the final orbit determination information solution and latest mesoscale atmosphere prediction to provide a best estimate of the entry performance before landing. These preflight predictions agree remarkably well with the reconstructed angles of attack and sideslip derived from the IMU. There are some deviations, which will be discussed later, but this comparison indicated that, in general, the capsule behaved much as
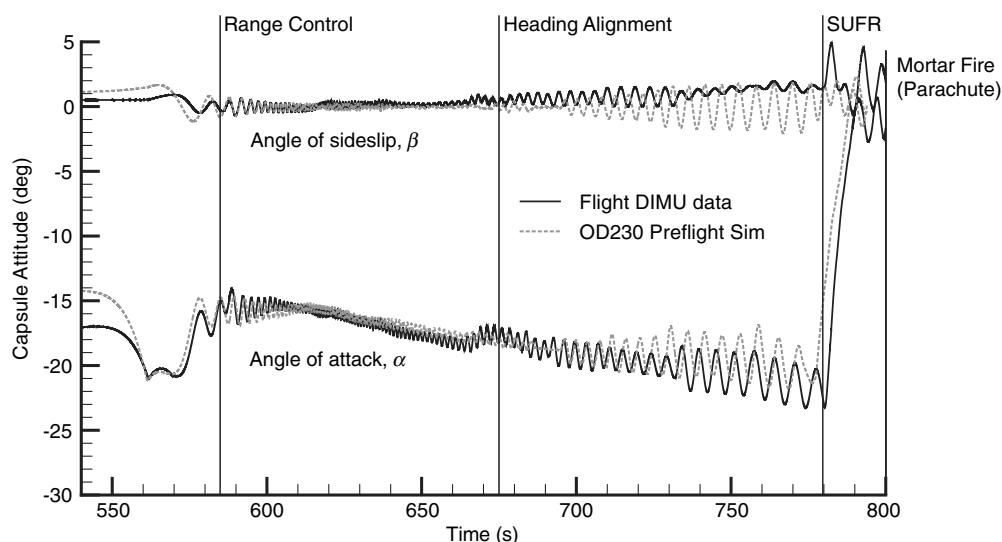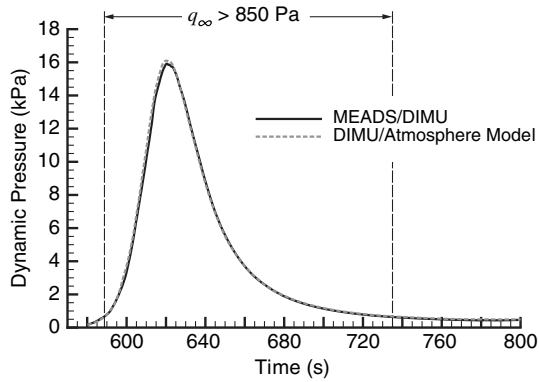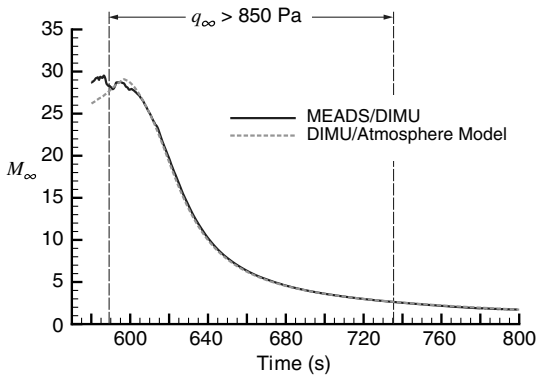

Fig. 6   Comparison of preflight and reconstructed angles of attack and sideslip.

a) Dynamic pressure

b) Mach number

Fig. 7   Reconstructed trajectory data.

a) OD230 simulation data

b) Flight data

Fig. 8   Comparison of RCS firing activity, last nominal simulation and flight data.

predicted. The reconstructed dynamic pressure and Mach number histories along the capsule entry trajectory using MEADS pressure measurements (anchored with the DIMU inertial velocity) are plotted in Fig. 7, compared with versions generated with DIMU measurements and a preflight atmosphere model. Both sets of data show close agreement and the differences are within the uncertainties of the measurement instruments and the preflight atmosphere model. Again, these comparisons show that the flight through the atmosphere was much as expected. The capsule attitude, velocity, and MEADS/DIMU Mach number were used to query the aerodynamic database. The MEADS/DIMU dynamic pressure with the DIMU acceleration measurements were used to extract the static aerodynamic coefficients from the flight telemetry (described later) to compare with the nominal database values.

1.   Reaction Control Firing History

Preflight simulation predictions of RCS firings are compared with the commands given during flight in Fig. 8. The roll, pitch, and yaw commands were calculated by summing all eight jets, assigning either a +1 or −1 contribution to that axis depending on the jet. For example, a value of +4 for the roll axis would indicate that four of eight jets are commanded to provide a positive roll torque and the remaining four jets are inactive. Summing the jets into these primary torque commands helps simplify the eight-jet firing history to see what actions the controller was requesting. The most notable events are the three bank reversals, indicated by a full bank command to start the rotation, immediately followed by a bank command of opposite sign to arrest the motion. Both the preflight and flight data indicate three reversals. In the flight data, the first reversal starts at 612 s, followed shortly after by another around 633 s. The third and final bank reversal occurs at 663 s. The 180 deg roll that occurs during SUFR is also evident starting at 780 s. In general, bank reversals in the flight data look much like preflight predictions. The flight data show less RCS activity away from the big bank commands than was predicted before entry. This will be discussed later.
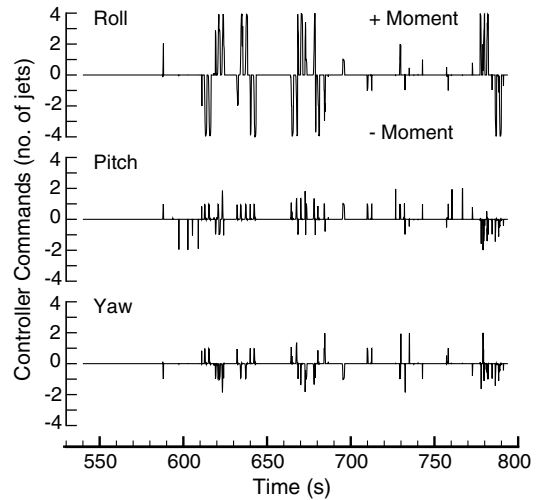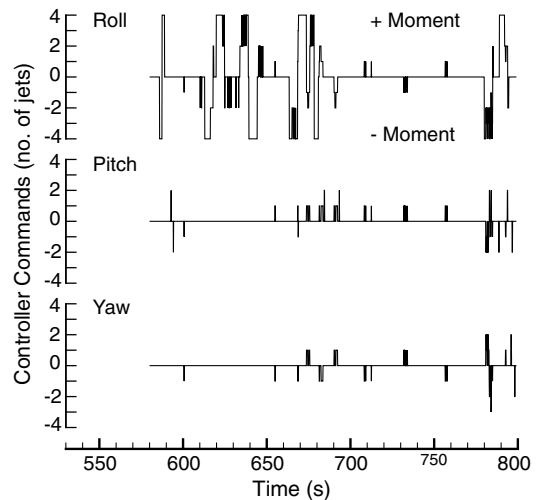
2.   Comparison of MEADS Pressures to LAURA CFD Solutions

To better appreciate the accuracy of both the trajectory data and aerodynamic coefficients extracted using the MEADS pressure measurements, it is important to compare the measured pressures to the "truth" model used to convert raw pressure measurements into the desired data products. The truth model was built from surface pressure distributions from the LAURA CFD solutions used to generate the MSL aerodynamic database. The CFD solutions are the best predictions of the pressure distributions expected during entry through the Mars atmosphere. There is the potential for the aerodynamic database coefficients and MEADS extracted parameters to be partially correlated because they both use the same sets of data. However, there are significant differences in how the information is used in database construction and parameter identification, so that the results are largely independent. The MEADS reconstruction of aerodynamic coefficients uses CFD to determine dynamic pressure only (together with independent accelerometer measurements in the DIMU), given the measured stagnation pressure. The dynamic pressure measurement is the most accurate parameter identified with MEADS pressures because it is dependent primarily on the stagnation pressure measurement only, with the LAURA CFD calculations being used only to determine the dynamic pressure upstream of the bow shock. CFD error away from the stagnation point does not affect the aerodynamic coefficient measurements.

The development of the LAURA code has included validation comparisons to stand-alone normal shock codes like CEA [21] and other chemically reacting Navier Stokes CFD codes. Such comparisons have shown that the ratio of dynamic-to-stagnation pressure calculated along the stagnation line in LAURA is as accurate as other computational methods for solving the hypersonic normal shock problem. Atmospheric density can then be calculated from a stagnation point measurement and the DIMU freestream velocity. Errors in the CFD solution across the MSL capsule surface, away from the stagnation point, do not affect the dynamic pressure/density calculations. Therefore, the dynamic pressure reconstructed from MEADS pressure measurements and the DIMU reconstruction is the most accurate data product. Aerodynamic coefficients within the aerodynamic database are obtained by integrating the computed pressure and shear stresses over the entire heat shield, whereas MEADS pressure predictions are extracted from the same CFD solutions at the discrete port locations. Errors in the computed pressure distribution away from the MEADS port locations become additional errors in the database coefficients. In other words, the MEADS pressures can be in close agreement with the CFD pressure coefficients at the MEADS port locations, yet the reconstructed aerodynamic coefficients can still be in disagreement with CFD predictions due to errors across regions of the heat shield away from the MEADS ports.

A comparison of the seven MEADS measurements to the CFD pressures at the converged state provides a qualitative and quantitative assessment of MEADS state measurements. Close agreement at each port location suggests that the flight pressure distribution is in good agreement with prediction. A large variation in fit quality among the MEADS pressures would suggest that the CFD pressure model did not properly predict the surface pressure distribution during flight, or that one or more MEADS transducers experienced

some kind of anomaly. The measured pressures are compared with the converged points in the CFD model in Fig. 9. The pressure data are presented as a pressure coefficient C_p defined as

$$C_p = \frac{p_i - p_\infty}{q_\infty} \qquad (3)$$

where p_i is a MEADS pressure measurement or local CFD pressure value, p_∞ is the freestream static pressure, and q_∞ is the freestream dynamic pressure. The CFD model is defined in terms of pressure coefficient. Nondimensionalizing the pressures in this manner eliminates variations due to trajectory differences, keeping the database a function of velocity or Mach and angles of attack and sideslip. Large deviations from the expected trajectory would introduce some errors, but analysis of the aerodynamic database shows that such errors are small for the MSL preflight and flight trajectories. The two plots in Fig. 9 are at supersonic and hypersonic conditions at angles of attack close to database CFD solutions. These plots are representative of the data fit quality during entry. Ports 6 and 7 are not shown but have similar agreement between measurements and the CFD model. The MEADS pressures follow the CFD pressure distribution closely at both conditions. Port 5 has the only notable variation away from the peak dynamic pressure pulse. Port 5 is located at a spot on the heat shield that sees a local pressure drop as flow around the capsule nose accelerates around the sphere cap to the leeward side of the forebody cone. The local pressure minimum moves on the heat shield surfaces as the capsule decelerates along the trajectory. CFD errors in predicting this local nonlinear phenomenon appear to be the largest disagreement between flight measurements and the model. The pressure residuals (CFD pressure at the converged point subtracted from the measured pressures) for each transducer are plotted in Fig. 10. The largest residuals occur at peak dynamic pressure because that is the time when peak absolute pressures are encountered. Even there, the residuals are generally under 100 Pa, which is less than 1% of reading.

To better illustrate the more pronounced variations of the port 5 residuals, the residuals of ports 2 and 5 are plotted on an expanded scale in Fig. 11. Port 2 is representative of the other ports along the centerline, where the residuals generally appear to be data noise with no systematic variations. Consistent with comparisons like those shown in Fig. 9, port 5 shows a long-term variation from the predicted model. After the dynamic pressure pulse, the port 5 residuals first indicate higher pressures than the CFD model, then drop below predicted near 725 s. The peak deviations (high and low) are roughly 1% of reading. Referring back to Fig. 10, across the peak dynamic pressure pulse (~590–640 s), ports 6 and 7 both show a dip below the model followed by an increase in C_p above predictions. These local variations hint at regions on the heat shield surface where CFD mispredicted the flight pressure distribution. The port 5 variation with time may be due to a discrepancy along the trajectory between
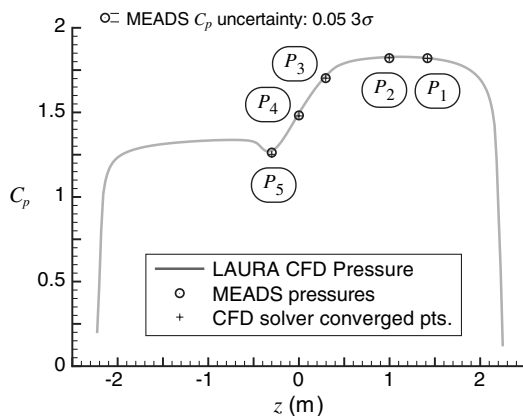
a) $M_\infty = 4.0$, $\alpha = -18.9$ deg
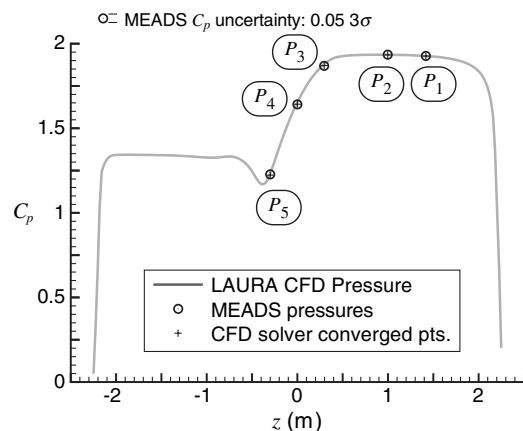
b) $M_\infty = 18.0$, $\alpha = -16.4$ deg

Fig. 9 MEADS pressures compared with CFD surface and converged CFD port values.
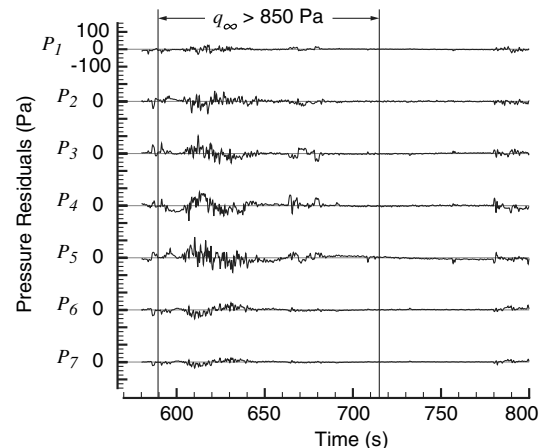

Fig. 10 Residuals of MEADS pressures measurements with converged CFD pressure model.
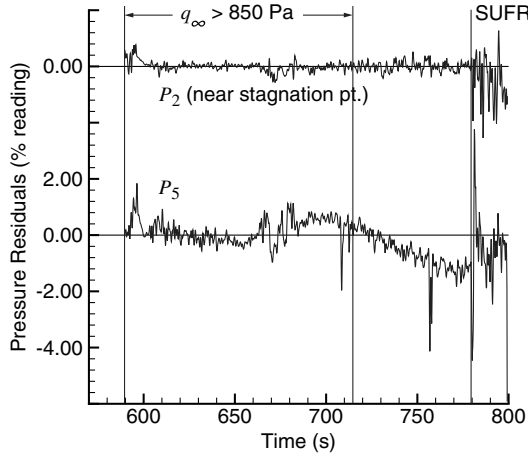
Fig. 11 Detail of residuals for ports 2 and 5, MEADS pressures fit to CFD model.

the predicted and actual location of the local pressure minimum downstream of the capsule nose. The symmetry of the residual signal for ports 6 and 7 also points to a minor discrepancy between the local pressures seen in flight and the CFD model. All variations are small, but this information may be used in future efforts to improve CFD codes by reconciling prediction with flight data. Overall, the agreement of MEADS and model pressures are excellent and add confidence in the reconstructed aerodynamic angles and dynamic pressure.

C. Extraction of Aerodynamic Forces and Moments

The dynamic pressure from the MEADS/DIMU reconstructed trajectory ($q_\infty = q_{\infty,\text{MEADS}}$) was used to extract aerodynamic forces. The aerodynamic forces were determined using the DIMU accelerometer measurements, rotated into the aerodynamic coordinate system (a_x, a_y, and a_z), with the measured entry vehicle mass m_{EV} and reference area S_{ref}:

$$C_A = -\frac{m_{\text{EV}} a_x}{q_{\infty,\text{MEADS}} S_{\text{ref}}} \tag{4}$$

$$C_Y = \frac{m_{\text{EV}} a_y}{q_{\infty,\text{MEADS}} S_{\text{ref}}} \tag{5}$$

$$C_N = -\frac{m_{\text{EV}} a_z}{q_{\infty,\text{MEADS}} S_{\text{ref}}} \tag{6}$$

The mass listed in Fig. 1 was the expected mass of the entry vehicle at entry interface based on prelaunch measurements. Before entry, the RCS system is used to despin the vehicle and turn to the proper orientation for entry. After interface, the RCS is used to perform bank reversals and damp rates. The commanded RCS firing history is known from telemetry but the fuel mass expended with each firing can only be estimated. The estimated total RCS propellant mass used during capsule flight was accounted for in the reconstruction process. As predicted, the fuel usage during EV flight was a small (∼0.5%) fraction of the vehicle mass at entry, and so a detailed mass accounting for each RCS firing was not done. Instead, the mass loss due to RCS firings from entry interface down to parachute deploy was removed from the vehicle mass linearly with time.

The static moments can be extracted from the flight telemetry and can also be assessed using the pitch and yaw frequencies of oscillation in the body rates and angle-of-attack and sideslip histories. First, the static moments can be measured using the DIMU angular rate information:

$$M_{\text{aero}} = I\dot{\omega} + \omega \times I\omega \tag{7}$$

where I is the measured moment of inertial tensor and ω is a vector of the measured angular rates. The angular acceleration vector $\dot{\omega}$ was determined by taking finite difference derivatives of the DIMU angular rates. The moment coefficients can then be determined by nondimensionalizing the measured moments by the MEADS/DIMU dynamic pressure and measured reference area and length:

$$C_l = \frac{M_{\text{aero},i}}{q_{\infty,\text{MEADS}} S_{\text{ref}} d_{\text{ref}}} \tag{8}$$

$$C_m = \frac{M_{\text{aero},j}}{q_{\infty,\text{MEADS}} S_{\text{ref}} d_{\text{ref}}} \tag{9}$$

$$C_n = \frac{M_{\text{aero},k}}{q_{\infty,\text{MEADS}} S_{\text{ref}} d_{\text{ref}}} \tag{10}$$

The capsule motion during entry showed small oscillations in angle of attack and sideslip and virtually no roll that was not commanded by the onboard controller. The RCS frequently disturbed the natural capsule angular rates and accelerations as bank maneuvers and rate damping jet firings were executed. Therefore, the moments measured directly from the rates and their derivatives are subject to significant errors. With only small oscillations about the trim point, there is little signal to noise. It was concluded that using Eq. (7) to measure moments and then extract the moment coefficients was not the best approach for the MSL configuration.

Two approaches were adopted to assess the vehicle stability and trim characteristics for more meaningful comparisons with preflight predictions. First, a simple comparison of the predicted trim angle to the reconstructed angle-of-attack history showed how well the preflight calculations predicted the static stability and how accurately the trim angle was prescribed by specifying a radial c.g. offset. The predicted trim angle, using the measured c.g. location and nominal aerodynamic database, were compared with the reconstructed angle-of-attack history. Second, the pitch and yaw frequencies of oscillation were compared with the natural frequencies expected from preflight predictions of the local static stability characteristics of the capsule. The capsule oscillations can be modeled as a damped harmonic oscillator. The capsule static stability provides the "spring stiffness" of the pitch and yaw oscillations. Damping adds a negligible contribution to the natural frequency, and so the predicted frequencies can be estimated with the static stability terms only. About the pitch plane, the expected frequency of oscillation is given by the following relation:

$$f_y = \frac{\omega_y}{2\pi} = \frac{1}{2\pi} \sqrt{-\frac{q_{\infty,\text{MEADS}} S_{\text{ref}} d_{\text{ref}} C_{m_\alpha}}{I_{yy}}} \tag{11}$$

where f_y is the pitch oscillation frequency in hertz. The derivative C_{m_α} is the local pitch stability slope (per radian) determined from the MSL aerodynamic database. I_{yy} is the measured moment of inertia about the pitch axis. Rearranging this equation, the local static stability can be calculated using the local oscillation frequency and dynamic pressure:

$$C_{m_\alpha} = -\frac{I_{yy} \omega_y^2}{q_{\infty,\text{MEADS}} S_{\text{ref}} d_{\text{ref}}} \tag{12}$$

In the data reduction here, the oscillation frequency was determined by fitting a sinusoidal wave through the pitch body rate q. Because RCS firings corrupt the natural frequency oscillations, segments of the trajectory free of RCS jet commands were selected to identify the natural frequency. Eight segments along the trajectory were identified where the capsule fired no RCS jets for a period of at least 2 s. The

pitch oscillation frequency was determined by fitting the following model to the body rate data over each of these eight segments:

$$q = A \cos(\omega_y t + \phi_y) + C \qquad (13)$$

The oscillation frequency ω_y was identified by fitting the model to the raw data and the static stability was extracted using Eq. (12) with the measured moment of inertia, reference dimensions, and the MEADS/DIMU dynamic pressure history.

Extracting the yaw stability C_{n_β} proved to be slightly more complicated. The added complexity arises from the fact that the yaw stability derivative is with respect to the sideslip angle β, whereas the most direct and accurate source of rate data is about the yaw body axis z, directly measured by the DIMU. The β axis of rotation is rotated out of collinearity with the body yaw axis by the trim angle of attack. There is also a small contribution to the sideslip oscillation by the periodic roll torque caused by the side force, produced by sideslip oscillations, acting at a distance from radially offset center of gravity. The complications of extracting 6DOF aerodynamic coefficients from an axisymmetric geometry being flown with a radial c.g. offset have been described in another paper by Schoenenberger et al. [22]. For a configuration like MSL at supersonic and hypersonic conditions, where heaving motions are small, the sideslip rate $\dot{\beta}$ can be expressed in terms of the roll and yaw rates p and r:

$$\dot{\beta} = p \sin \alpha_{\text{Trim}} - r \cos \alpha_{\text{Trim}} \qquad (14)$$

Schoenenberger et al. show the frequency of oscillation about the z axis is then

$$f_z = \frac{\omega_z}{2\pi} = \frac{1}{2\pi} \sqrt{\frac{q_{\infty,\text{MEADS}} S_{\text{ref}} d_{\text{ref}} C_{n_\beta}}{I_{zz}} \frac{\dot{\beta}}{r}} \qquad (15)$$

The expression for $\dot{\beta}$ is then substituted into Eq. (15). It can be shown that the $(p/r) \sin \alpha_{\text{Trim}}$ term is negligible for the MSL configuration. Therefore, the frequency about the body z axis becomes

$$f_z = \frac{\omega_z}{2\pi} = \frac{1}{2\pi} \sqrt{\frac{q_{\infty,\text{MEADS}} S_{\text{ref}} d_{\text{ref}} C_{n_\beta} \cos \alpha_{\text{Trim}}}{I_{zz}}} \qquad (16)$$

I_{zz} is the measured moment of inertia about the z axis. After rearranging, the expression for extracting the yaw static stability coefficient becomes

$$C_{n_\beta} = \frac{I_{zz} \omega_z^2}{q_{\text{MEADS}} S_{\text{ref}} d_{\text{ref}} \cos \alpha_{\text{Trim}}} \qquad (17)$$

This expression is similar to that for C_{m_α}, except for the factor of $1/\cos \alpha_{\text{Trim}}$. For this analysis, α_{Trim} was determined by fitting the DIMU angle of attack to a model similar to those used to fit the body rate data [Eqs. (13) and (18)]. For such a model, the constant term added to the periodic term is the value of the trim angle of attack:

$$r = B \cos(\omega_z t + \phi_z) + D \qquad (18)$$

The frequency of oscillation about the z axis ω_z was determined by fitting the model described by the preceding equation to the DIMU yaw rate at the quiescent points (no RCS firing) identified along the trajectory. The expressions in Eqs. (12) and (17) were used to extract the pitch and yaw stability.

An attempt was made to extract the frequencies across the entire entry as well. The capsule pitch and yaw frequencies (oscillation frequencies about the vehicle center of gravity) were extracted from a time-frequency (TF) analysis of the DIMU data. This analysis used MATLAB routines from the Time-Frequency Toolbox.[†† ,‡‡] This

toolbox makes use of a TF method, referred to as "reassignment," which improves the readability of TF distributions [23]. As with the analysis of the quiescent segments, the signals used in this analysis were yaw and pitch rates (about the body y and z axes) from the raw DIMU telemetry. Signals were downsampled by interpolation to regular 12 Hz intervals, allowing 4096 (2^{12}) frequency bins over approximately 340 s of the trajectory, which is sufficient to capture the entire entry deceleration pulse (approximately 213 s) as well as the full time on parachute (approximately 117 s). An assessment of the results showed that the RCS firing affected the resulting frequencies extracted. Also, finite windows of data were required to evaluate and extract the frequencies. In regions where the dynamic pressure was changing rapidly, the window size had a noticeable effect on the extracted frequencies. Qualitatively, the extracted frequencies agreed well with those predicted by the static stability in the aerodynamic database. However, the accuracy of the TF technique appeared to be on the order of the aerodynamic database uncertainties. Therefore, the method of identifying the frequency across more discrete periods of no RCS activity was selected as the most accurate for comparison with predictions. The time-frequency results agree with these data to within the accuracy of the method, but end up providing no additional quantitative information. The TF results will not be shown here.

1. Uncertainty Analysis and Sources of Error

A significant portion of the MEADS reconstruction development was the identification and quantification of the uncertainties in measuring the MEADS parameters. This activity included assessing pressure transducer and DIMU accuracy, installation tolerances, lag times, and many other sources. A matrix of all error sources was established for the certification of the MEADS experiment for flight. It was shown that the installed instrumentation has the accuracy to resolve the dynamic pressure to within 2% and angles of attack and sideslip to within 0.5 deg (for $q_\infty > 850$ Pa), assuming the CFD-based pressure model perfectly predicted the flight surface pressures. The largest source of uncertainty in the MEADS measurements was found to be the CFD pressure model used as truth to convert the measured pressures to angles and dynamic pressure. An extensive CFD calibration campaign, using wind-tunnel pressure tests, was undertaken to help quantify the local surface (MEADS port) uncertainties in CFD solutions. However, the test accuracy tended to be on the order of the uncertainties carried for the CFD solutions. Although the testing could not reduce the CFD pressure uncertainty model, they did provide confirmation that the model uncertainties were of the right order. CFD analysis was run to assess uncertainty effects due to grid resolution, heat shield ablation, deformation, outer mold line shape knowledge, and hole location knowledge error. It was found that, for each port, the computational accuracy of the CFD database was good to about 0.5% of the measured pressure coefficient or better. In addition, errors due to instrumentation, sampling, and hardware installation were included in the uncertainty models. These error sources include transducer calibration uncertainties, hysteresis, system noise, transducer temperature uncertainties, pneumatic lag, sample time tag errors, and pressure port location uncertainties. The total error for each point is modeled in the MEADS reconstruction algorithm, which uses a nonlinear least-squares algorithm to solve for the atmospheric data states. This algorithm produces an estimate of the uncertainties in the reconstructed states from the covariance matrix. Monte Carlo analyses were conducted to verify that the estimated uncertainties based on the covariance were accurate. The distribution of the reconstructed parameters is approximately Gaussian. In preflight analysis, the CFD pressure model dominated all hardware and installation sources of error.

Accelerations and angular rates used for the aerodynamic coefficient reconstruction were based on the raw 200 Hz DIMU data, which were smoothed using a Tustin bilinear filter. The uncertainties in the filtered acceleration and rate data consist of systematic errors (bias, scale factor, misalignment) from the DIMU specifications and an estimate of the residual noise and errors due to the filtering artifacts, such as lag or ringing. These uncertainties were estimated from the data from the POST2 simulation that used flight software and a model

---

††Developed by the Centre National de la Recherche Scientifique (CNRS).
‡‡Data available online at http://tftb.nongnu.org/ [retrieved 28 May 2014].

a) Dynamic pressure and axial force coefficient
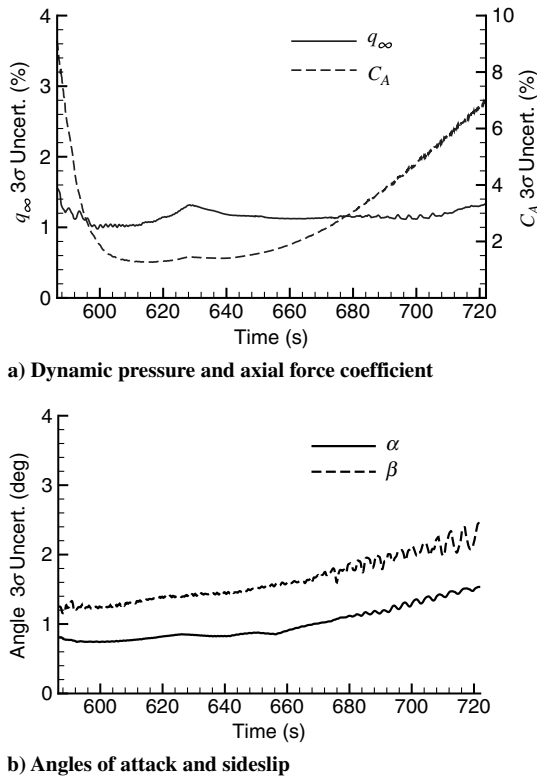

b) Angles of attack and sideslip

Fig. 12 MEADS/DIMU uncertainties.

of the DIMU. Filtered data were compared with truth and an estimate of errors including residual noise and filtering artifacts was computed.

The 3σ uncertainties from the MEADS/DIMU reconstruction for the portion of the trajectory where dynamic pressure is greater than 850 Pa are plotted in Fig. 12. The 3σ values for the MEADS parameters were determined within the solution algorithm, as described earlier. The 3σ curve for C_A captures the uncertainty contributions from the axial accelerometer (which includes the filter effects, as described earlier), MEADS dynamic pressure, mass, and measured reference area. The uncertainty distributions for these parameters are not known, but the good agreement between the nonlinear least-squares algorithm and the Monte Carlo analysis described earlier indicate that a Gaussian assumption is a reasonable approximation. The curves show the increase in uncertainty, above the instrumentation system uncertainties, due to the CFD uncertainty model. In practice, the good convergence of MEADS flight measurements to the CFD model suggests the preflight uncertainty models may be conservative. However, these uncertainty curves do provide reasonable bounds for the uncertainties of the reconstructed dynamic pressure, angle of attack and sideslip, and axial force coefficient. The dynamic pressure uncertainty remains fairly constant, between 1 and 1.5% over the entire portion of the trajectory for which the MEADS experiment was designed. The axial force coefficient uncertainty is slightly greater than the dynamic pressure uncertainty near peak dynamic pressure where the accelerometer signal to noise is high. At lower dynamic pressures (both early and late in the timeline), accelerometer noise adds to the uncertainty significantly.

In addition to the filter study using POST2 simulations with a model of the DIMU, a study of the effect of different filters on reconstructed C_A history was performed on the flight data. Several

filters were applied; each filter generally collapsed the reconstructed data to a consistent mean C_A history, with the local filter-driven signal remaining in the results. The study indicated that the Tustin filter provided a reasonable smoothing of the raw data. Because this filter was used by other groups within the MSL entry, descent, and landing (EDL) team and there was no significant improvement identified using the other filters, the Tustin filter was used. One problem observed with all of the filters was finding a robust approach to remove the accelerations produced by RCS firings. In the end, no satisfactory approach was identified and the RCS firings are left as an additional error source in the filtered accelerometer data used to extract aerodynamic coefficients. Because the RCS jet thrust magnitudes are constant, their contributions to the aerodynamic coefficients are inversely proportional to the dynamic pressure. Areas where the RCS jets introduce noise in reconstructed parameters will be discussed in the results section.

2. Reconciliation of Predicted and Reconstructed Aerodynamic Coefficients

The MSL aerodynamic database uncertainties were modeled for use in Monte Carlo analysis to assess the sensitivities of the entry descent and landing system to off-nominal aerodynamic performance. The uncertainty model consists of a set of adders and multipliers applied to each aerodynamic coefficient [11]. The uncertainties were defined for three different flight regimes: rarefied/transitional, hypersonic continuum, and supersonic continuum. For each Monte Carlo case, a random dispersion for each uncertainty value was applied, dispersing the aerodynamic coefficients by a constant fraction of the defined 3σ values for each flight regime. For example, consider the dispersion equations for the axial and normal force coefficients:

$$C_{A_{\text{Disp}}} = C_A(\alpha, \beta)(1 + U_{C_A}^M) \tag{19}$$

$$C_{N_{\text{Disp}}} = [C_N(\alpha, \beta) + U_{C_N}^A](1 + U_{C_N}^M) \tag{20}$$

where $U_{C_A}^M$ is a multiplier applied to the nominal axial force coefficient, and $U_{C_N}^A$ and $U_{C_N}^M$ are adder and multiplier dispersions applied to the normal force coefficient. The 3σ magnitudes of the adders and multipliers for each coefficient used in the MSL aerodynamic database are listed in Table 1. The values were determined by comparisons of the database CFD solutions to wind-tunnel data (heritage Viking wind-tunnel data and new MSL test data) and recent flight data (Mars Pathfinder, Mars exploration rovers, and Mars Phoenix). Sensitivity studies looking at gas models within the CFD codes, grid resolution, ablation, and deformation, etc. were also conducted. Ultimately, engineering judgment determined the final values because there are "unknown unknowns" associated with the flight vehicle flying through the Mars atmosphere that cannot be accounted for before flight.

After comparing the aerodynamic database values, queried at the reconstructed trajectory states, to the MEADS/DIMU extracted coefficients, a set of dispersion values that best reconciled the aerodynamic database values with the reconstructed values were identified using least-squares fits. For the aerodynamic force coefficients, the uncertainties were determined by fitting the aerodynamic database model to the extracted coefficients. For the moments, adder dispersions were identified by fitting the database trim angle to the reconstructed angles of attack and sideslip. The moment multipliers were determined by fitting the local static stability to the values extracted using the body rate data at the no-RCS segments of the

Table 1 Static aerodynamic uncertainties, 3σ

Coefficient	C_A	C_N, C_Y	C_m	C_n	C_l
Uncertainty	$U_{C_A}^M$	$U_{C_N}^A, U_{C_N}^M$	$U_{C_m}^A, U_{C_m}^M$	$U_{C_n}^A, U_{C_n}^M$	$U_{C_l}^A$
Knudsen > 0.1	±5%	±0.01, ±10%	±0.005, ±20%	±0.005, ±20%	0.0009
Mach > 10	±3%	±0.01, ±10%	±0.006, ±20%	±0.003, ±20%	0.000326
Mach < 5	±10%	±0.01, ±10%	±0.005, ±20%	±0.005, ±20%	0.0004

trajectory. The identification of the best-fit uncertainty values was done for the hypersonic and supersonic dispersions. The low-density transitional flight regime was outside the valid range of the MEADS transducers and that comparison is not assessed in this work. The identified dispersions give an estimate of how greatly the measured aerodynamic performance differed from the nominal preflight values.

III. Results

The trajectory reconstruction results using DIMU and MEADS data are presented here and compared with the MSL aerodynamic database. First, the angles of attack and sideslip are revisited with the reconstructed lift-to-drag performance to show how the EV flight performance compared with prediction. Then, the individual aero-dynamic coefficients are compared and assessed. Some qualitative comments supported by data from the reconstructions will be given to address some parameters that could not be extracted explicitly (dynamic stability, RCS aerodynamic interactions, etc.). The reconstruction process as described by Karlgaard et al. [19] was quite successful and the MSL project is confident in the interpretation of these results. Some minor anomalies have been identified, which will be discussed, but overall, the MSL entry capsule performance was very close to predictions.

A. Entry Performance

In Fig. 13a, the DIMU reconstructed angle of attack is compared with the preflight predicted trim angle (using the measured c.g. location and MEADS/DIMU Mach and velocity states along the trajectory). Note that, in this figure and in many to follow, the MEADS experiment boundaries ($q_\infty = 850$ Pa) are labeled. The DIMU-reconstructed α history agrees well with preflight predictions, matching the predicted trim angle almost exactly over much of the hypersonic regime. At the initial entry velocity, the reconstructed angle is smaller (less negative) than the preflight predicted trim angle. This was expected because CFD (and direct simulation Monte Carlo data used early in the trajectory) had been calculated at conditions along a preliminary MSL trajectory. Early in the entry, the aero-dynamic coefficients are somewhat sensitive to the freestream density in addition to the freestream velocity, which is used as the independent variable in the database. The errors early in the trajectory are due to a mismatch between the flight trajectory and the conditions at which the database points were run. During database development, it was decided by the MSL project that these small errors were not worth correcting with updated CFD solutions. The dynamic pressure is small in this region and the errors were easily "flown out" by the onboard guidance, resulting in no significant fuel or landing accuracy penalty when evaluated in simulation. On the other side of the dynamic pressure pulse, there is a small departure in the DIMU α near Mach 6. This occurs during the final bank reversal. The DIMU is unaware of the wind environment through which the capsule is flying. This angle departure is consistent with the expected response of the DIMU if the capsule performed a bank reversal maneuver through a crosswind on the order of 10–20 m/s.

Detail of the DIMU-based angle of attack at low supersonic speeds, along with the MEADS reconstructed version, is shown in Fig. 13b. Note that the MEADS reconstruction search algorithm used the Mach number determined by the DIMU-based freestream velo-city and freestream temperature based on a hydrostatic atmosphere reconstruction. Both angle-of-attack reconstructions are in good agreement with each other as well as preflight predictions. Just above Mach 2.0, the SUFR maneuver is performed, where six tungsten balance masses are jettisoned to move the center of gravity to the spin axis of the vehicle, reducing the trim angle to 0 deg. While the masses are being jettisoned, a sequence of RCS jet firings occur to bank the vehicle 180 deg to prepare for radar measurements later in the entry timeline. The flight data show that the change in trim angle occurred with little oscillatory excitation. Neither the bank maneuver nor mass jettisons appeared to induce any unintended dynamics. Overall, the flight performance during SUFR was close to predictions.
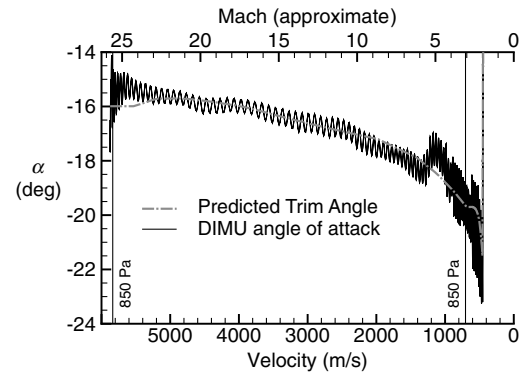
a) Entry angle of attack
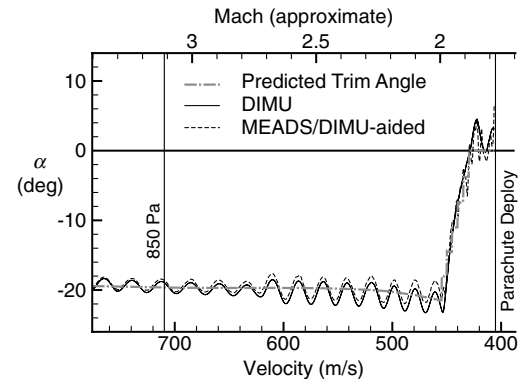
b) Supersonic detail

Fig. 13   Predicted and reconstructed trim angle of attack.

Figure 14 shows the difference between the DIMU and MEADS angle-of-attack reconstructions over the entry trajectory. Over much of the hypersonic segment of the trajectory there is a constant offset of approximately 0.4 deg between the two reconstructed angles. Uncer-tainty analysis and the accuracy of the overall inertial reconstruction of the vehicle trajectory down to the landing site [19] indicate that the DIMU angle is more accurate. The difference between the two is well within the calculated accuracy of the MEADS measurements and CFD model. Unknown atmospheric winds are a source of error but any realistic wind velocity is a small fraction of the freestream velocity of the EV at hypersonic speeds. As mentioned earlier, near Mach 6, the vehicle completed its last bank reversal, and subsequent reconstruction analysis showed that the observed angle of attack is consistent with the maneuver being done in a crosswind. At roughly Mach 6.0 and below, unknown winds begin to contribute to DIMU angle-of-attack errors. The steady increase in the difference between DIMU and MEADS α starting near Mach 5 is consistent with a
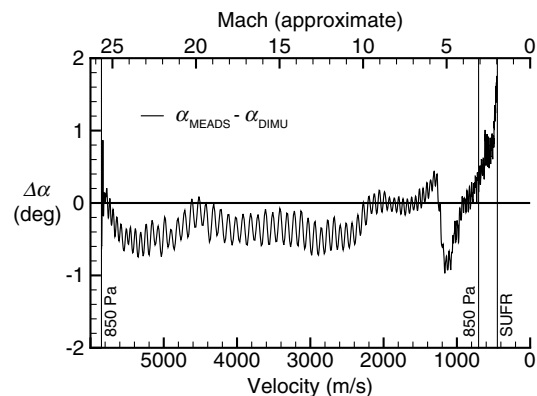

Fig. 14   Difference between angle of attack reconstructed from MEADS and DIMU.

roughly steady tailwind that becomes a larger and larger component of the freestream velocity as the vehicle decelerates. Karlgaard et al. solved for the wind profile by differencing these wind relative and inertial angles [19]. For the purpose of assessing the preflight aerodynamic predictions, these differences are small and not corrected for here. For subsequent plots, the DIMU angle of attack was used to query the preflight aerodynamic database to compare with reconstructed aerodynamic coefficients because that angle is more accurate over a larger segment of the trajectory. Which angle of attack was used to query the database did not affect the overall conclusions drawn regarding the comparisons of preflight predictions with the reconstructed aerodynamic behavior of the vehicle.

The lift-to-drag ratio, determined from the MEADS dynamic pressure and accelerometer measurements, is compared with the preflight prediction in Fig. 15. The reconstructed performance was just slightly under predictions ($\sim$1–4%) in the region of the trajectory where dynamic pressure was greater than 850 Pa. This again is remarkable agreement over the entire entry and well within the dispersions used for trajectory design. The difference between prediction and flight early in the trajectory is again due to a mismatch of flight freestream conditions and those used in the preflight CFD predictions. At lower speeds, agreement continues to be quite good. The most noticeable anomaly is the rise then dip of the mean C_L/C_D curve near Mach 6. This dip occurs during the final bank reversal and is tied to the reconstructed DIMU angle-of-attack history described earlier. Unlike the axial and normal force coefficients that are derived directly from DIMU accelerations, the lift and drag coefficients must be rotated into the wind frame, using the DIMU reconstructed angle of attack which includes the dip near Mach 6. Despite the introduction of angle-of-attack error, the lift-to-drag performance has been found to be well within predictions.

The sideslip reconstructions are plotted in Fig. 16. The data are only plotted until the start of the SUFR maneuver. As the SUFR balance masses are jettisoned, there are accelerations that introduce noise in the instrument measurements and small c.g. offsets that introduce significant sideslip dynamics compared with the nominal trim angle of $\beta = 0$ deg. Extracting the detailed attitude history during SUFR is beyond the scope of this work. However, before SUFR, drift in sideslip angle was noted in both the DIMU and MEADS reconstructions. Analysis has shown that the deviation from the expected near-zero sideslip angle identified by these two reconstructions is due to different phenomena. A third reconstruction of sideslip using the DIMU accelerometers and aerodynamic database has been added to support the interpretation of the data in total. Because the differences between the three curves are small and would be difficult to discern plotted on the same axes, the curve are presented offset from each other with each $\beta = 0$ deg line labeled.

The lateral c.g. offset is essentially zero and therefore no significant sideslip angle was expected. Both the DIMU and MEADS/DIMU reconstructions show a departure in sideslip angle reaching mean values of approximately 1.5–2 deg at SUFR. As shown earlier, the MEADS angle uncertainties are larger than the beta values shown
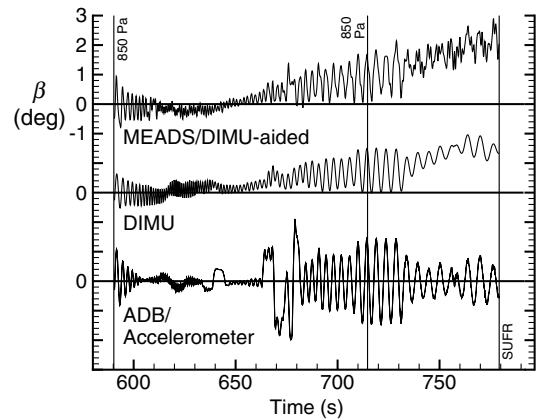

Fig. 16 Comparison of angle-of-sideslip reconstruction results.

here. Measurement error in port 6 or 7 is believed to explain the MEADS divergence. However, the inertial reconstruction of sideslip would not be expected to follow the MEADS results because an IMU cannot detect wind-relative information. The third attitude measurement method was added to provide more insight to this anomaly. The ratio of side force to axial force (C_Y/C_A) was matched with the ratio of transverse to axial acceleration (a_y/a_z) along the trajectory to find the sideslip angle using the MSL aerodynamic database. The results from this method show that the accelerometers measured no significant sideslip. It is difficult to identify a single phenomenon that reconciles these three versions of the sideslip angle. The MEADS and accelerometer measurements both reconstruct a wind-relative attitude. If MEADS measured a true sideslip divergence, due to a damaged heat shield or other "bent airframe" anomaly, the accelerometers should detect nonzero transverse accelerations as well. Postflight analysis suggests a combination of flight through a crosswind and MEADS measurement error, well within the transducer performance requirements, is the most likely explanation of the reconstructed sideslip angles.

As described in the reconstruction paper by Karlgaard et al. [19], the sideslip growth indicated by the MEADS data appears to be the result of a hysteresis in the pressure transducer signals. A constant correction of approximately 25 Pa to either port 6 or port 7 (decrement to port 6 or increment to port 7) was shown to reconcile the MEADS sideslip angle history with the accelerometer sideslip reconstruction. A review of calibration data of the flight transducers showed that each exhibited some amount of hysteresis response consistent with this port-6/port-7 difference as they were cycled through pressure pulses similar to those experienced in flight. Differences between pressure readings from the increasing and decreasing sides of a pressure pulse were on the order of 30–50 Pa. The variation of the hysteresis loops were different for each transducer and varied significantly depending on the durations of the pressure cycles and the temperatures at which the calibration runs were executed. The data were not of sufficient consistency to describe the hysteresis effects with a simple model for each transducer. The calibration data did show that it is quite possible, if not expected in hindsight, that the variation of hysteresis loops would result in errors on the order of 20–30 Pa between transducers. Because sideslip is primarily sensitive to the two lateral transducers, any differences in their hysteresis characteristics directly affect the measurement of β. In contrast, because angle of attack is measured primarily with a combination of the five transducers located along the pitch plane of the EV, variation in response from any one transducer is weighted less. Postflight analysis showed that the same magnitudes of hysteresis would result in approximately half the error in angle-of-attack measurement.

The pressure transducer hysteresis hypothesis does not explain the DIMU-reconstructed sideslip divergence. Again, the Karlgaard et al. [19] EKF reconstruction extracted winds that point to the likely explanation for the DIMU β divergence. A crosswind from north to south (the MSL capsule was traveling almost due east heading to the landing site) of approximately 10–20 m/s would have produced the
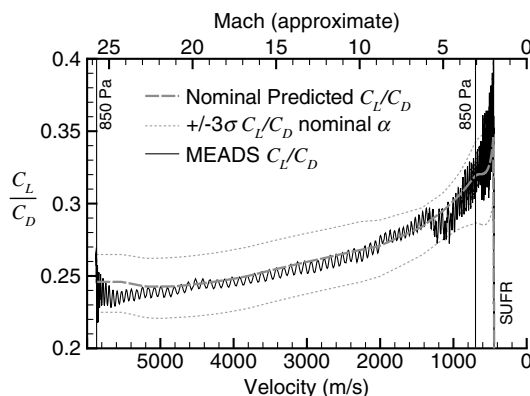

Fig. 15 Predicted and reconstructed lift-to-drag ratio.

DIMU sideslip measurement. Unaware of the wind environment, such a crosswind would cause a southward drift from the desired ground track to the landing site. Upon completion of the capsule's bank reversals used to control how far downrange the vehicle would travel, the capsule switched to a heading alignment mode where it directed the vehicle to fly along a heading toward a specific point on the planet using onboard inertial navigation. Any heading drift measured by the DIMU would result in a commanded bank to use the capsule's lift to maintain a proper heading. Being stable, the capsule would nose into the wind, trimming at $\beta = 0$ deg as the ADB/accelerometer reconstruction indicates. The DIMU-reconstructed sideslip angle is really the crab angle or heading adjustment required to maintain the desired heading to the landing target.

This crosswind explanation for the DIMU sideslip angle history is supported by onboard information. The commanded bank angle history during the heading alignment phase of entry is shown in Fig. 17. The onboard navigation filter's estimate of bank error is also shown. During heading alignment, the vehicle nominally instructs the EV to fly lift up (bank angle = 0 deg) with the controller ignoring bank errors within a ± 5 deg deadband. The bank angle error shows the vehicle gently rotating between the two deadband limits. Small RCS corrections are made when the deadbands are reached (refer back to Fig. 8b) and these are the only RCS firings during the heading alignment phase. Initially, the controller commands a large bank angle of -30 deg to clean up the heading errors incurred during the range control phase of entry. Then, instead of flying at pure lift-up orientation, the vehicle is commanded to fly at a small bank angle of approximately -2.5 deg (counterclockwise about the velocity vector when looking upwind at the vehicle) to maintain the desired heading to the landing target. Note that the sinusoidal variation of the commanded bank angle is to correct the vehicle heading as it meanders, while slowly rotating between the bank deadbands. The small nonzero mean bank command is consistent with the attitude required to crab into the north-to-south crosswind identified in the Kalman filter reconstruction. This crab angle then shows up as a small sideslip angle in the DIMU attitude estimate because the wind environment is unknown. The magnitude of the crab angle is consistent with simulations run after landing with varying crosswind magnitudes.

B. Static Forces and Moments

Comparisons of the static forces and moments extracted from the MSL flight trajectory with the MSL preflight aerodynamic database, queried at the reconstructed trajectory points, are presented in Figs. 18–23. Some figures show the reconstructed data differenced with the database values queried along the trajectory. This is done to provide a better visualization of the differences between preflight predictions and flight data. Most of the differences proved to be small and some are difficult to discern when the aerodynamic coefficients are plotted on top of each other. Three-sigma aerodynamic database dispersions (POST2 simulations model the dispersions with

Gaussian distributions) are also plotted to help visualize the degree to which the reconstructed aerodynamic coefficients differ from the nominal values in the preflight aerodynamic database.

1. Axial Force Coefficient

The axial force coefficient data are shown in Fig. 18. The aerodynamic database was queried at both the MEADS and DIMU angles-of-attack to assess the variation due to error in determining the capsule attitude. In Fig. 18, the preflight data queried at the DIMU angle of attack is shown. The differences between the MEADS and DIMU angle-of-attack histories are small and the DIMU version was selected to query the aerodynamic database for comparison to the MEADS/DIMU reconstruction of the aerodynamic coefficients. The difference of MEADS and preflight C_A data is shown in Fig. 19a across the hypersonic regime as a percent of the preflight prediction. Postflight analysis identified a best fit of the aerodynamic dispersions, which reconciled the flight data with the preflight model. This best-fit curve is also included in Fig. 19a. This dispersed version of the aerodynamic database shows two things. First, the flight data differed from predictions by only a little over 1% in the hypersonic regime. Second, the disagreement is fairly constant over the entire hypersonic regime. Put another way, the overall difference between reconstructed and predicted C_A is quite small and the local variation of the flight data from the best-fit curve is also small. The preflight uncertainty bounds look to have been good estimates and the use of a single-scale factor for the C_A dispersion model appears to replicate the first-order discrepancies.

The supersonic error is plotted in Fig. 19b. This plot shows a small increase in the error as the vehicle slows to supersonic speeds. The best-fit dispersed version of the database is again plotted. Within the MEADS experiment design space ($q_\infty > 850$ Pa), the disagreements are small and follow the dispersion model reasonably well. At dynamic pressures below 850 Pa, the flight data departs from prediction significantly. This will be discussed later. The C_A dispersions, used to generate the best-fit curves in these plots, are provided in Table 2. That table will be discussed in detail later as well.

A postflight effort was undertaken to identify potential sources of error that could reconcile the aerodynamic database and reconstructed C_A within the MEADS reconstruction space ($q_\infty > 850$ Pa). Referring to Eq. (4), there are several sources that could contribute to errors in the measured C_A. The success of the inertial trajectory reconstruction down to the final landing site suggests that the accelerometer error was small. The MEADS algorithm that fits pressure data to LAURA CFD predictions ensures that the dynamic pressure used to reconstruct C_A is consistent with the dynamic pressure in the CFD predictions. There is no indication that the heat shield was damaged, and so the measured reference area should be correct. This leaves the mass as the remaining variable that may differ from what was measured. To reconcile a 1% difference in C_A would require an error in capsule mass of approximately 31 kg lighter than it was when last measured. The mass of the entry vehicle was measured just before being stacked on the launch vehicle after final assembly at NASA Kennedy Space Center. For there to be a significant error, mass must have been lost after launch. Two possible mass-loss sources have been identified. It is possible that water that had been absorbed by the PICA heat shield tiles, and perhaps the backshell thermal protection system, outgassed during the cruise from Earth to Mars. The heat shield was kept in a climate-controlled environment from fabrication to launch, and so it is not likely that the heat shield absorbed a large amount of water. However, tests have been done for the Orion project to measure how much water PICA can absorb, so it is a known concern. Also, though recession was thought to be less than predicted, the mass loss during entry due to ablation was not accounted for. Coincidentally, conservative upper bounds for both water outgassing and ablation provided by MSL project members are both about 7–10 kg each. So, at best, a mass error could reconcile 2/3 of the observed difference in C_A. There is no way to determine mass loss due to either mechanism, but this helps give an idea of the accuracy of the reconstructed value.

Another possible source of error was in the CFD predictions of C_A. To reconcile the predicted and reconstructed values, the pressure
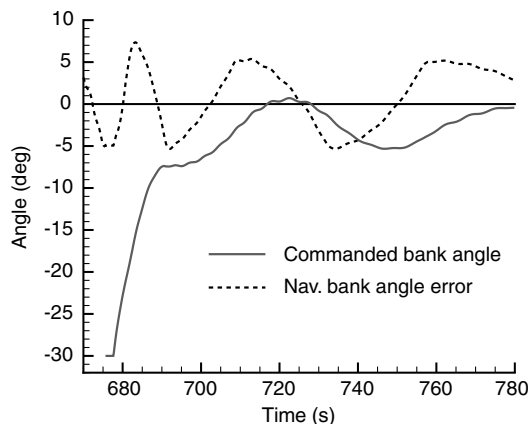

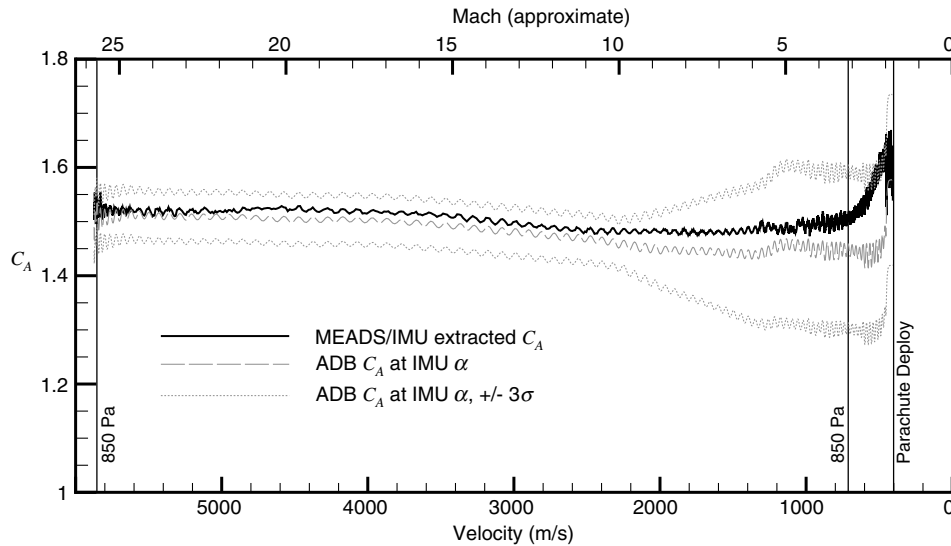**Fig. 17 Commanded bank angle during heading alignment.**

Fig. 18   Comparison of aerodynamic database C_A to reconstructed values.

distribution away from the MEADS ports would have to have differed from what was experienced in flight. The MEADS algorithm ensures that the pressure coefficients at the MEADS ports are in close agreement (the residuals in Fig. 10 confirm this), and so only differences in the pressures away from the MEADS port locations could lead to a difference in the predicted and reconstructed C_A values. It was hypothesized that improving the resolution of the shock structure with more tailored cell clustering, as well as doubling the grid resolution overall, might increase the pressures across the surfaces near the capsule shoulder. Additional CFD runs were made at conditions replicating conditions in the NASA Langley 31 in. Mach 10 tunnel with these grid improvements, and this was found to

be the case. There was an overall increase in C_A of approximately 0.66% but the stagnation pressure increased by 0.34% in the same solutions. The change in stagnation pressure would affect the MEADS-reconstructed dynamic pressure, essentially increasing C_A by the percentage increase of stagnation pressure. Therefore, the net reconciliation from the grid refinement is about 1/3%.

These sources of error all trend toward reconciling the discrepancy between the measured and predicted axial force coefficient. It is not believed that mass loss due to water outgassing and ablation could account for the full difference and, without measurements, it is unknown if either were significant. Postflight CFD analysis suggests that improved CFD grids could still provide a better prediction of the flight axial force coefficient. It should be emphasized that these remaining errors are small and the reconstructed axial force coefficient history is close to predicted.

As mentioned earlier, the most notable C_A disagreement occurs outside the MEADS dynamic pressure boundaries, leading up to the SUFR maneuver. The MEADS C_A increases significantly in the low supersonic regime. More details of this MEADS C_A anomaly is shown in Fig. 19b. The percent difference between the MEADS C_A and the nominal preflight prediction is shown along with the best-fit dispersions and the upper 3σ dispersion bound. The best-fit dispersion was determined using the segment of the trajectory within the MEADS dynamic pressure range. Beginning right as the capsule slows below the 850 Pa dynamic pressure point in the trajectory ($\sim$715 s) there is a noticeable divergence of the MEADS
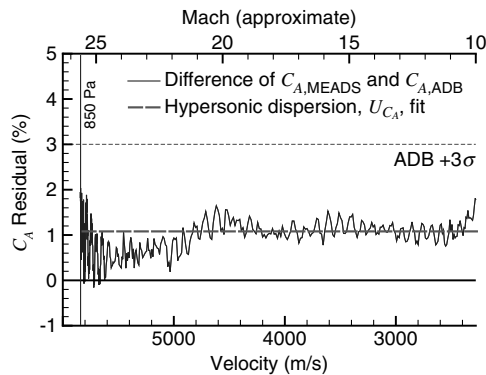
a) Hypersonic residuals
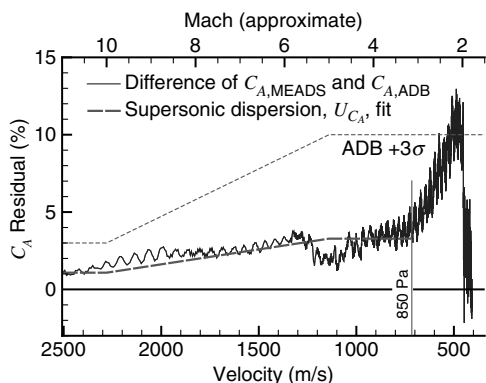
b) Supersonic residuals

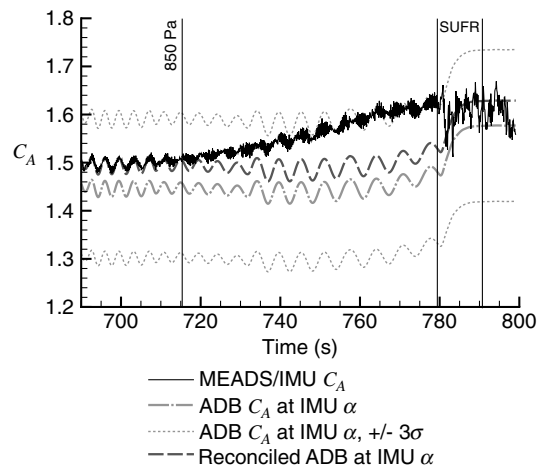Fig. 19   Detail of C_A comparison in hypersonic and supersonic regimes.

Fig. 20   Detail of C_A in supersonic regimes.

reconstructed C_A from both the nominal and best-fit dispersed aerodynamic database curves. It was first thought that the backshell contribution to axial force was different than the Viking flight data upon which correction was based [12], and a modification to the modeled base correction might reconcile this anomaly. However, a higher-than-expected axial force coefficient is at odds with the trajectory timeline. The time of entry extended longer than preflight simulations predicted in this region (see Fig. 6). In addition to the crosswind mentioned earlier, it is suspected that the capsule flew through a reasonable tailwind (10–20 m/s). This again is supported by the EKF reconstruction by Karlgaard et al. [19]. If the axial forces slowing the vehicle were greater than predictions, this would require an even greater tailwind or density drop to produce the flight trajectory that was reconstructed. With no base pressure measurements, it cannot be known whether the degree to which the Viking correction was incorrect for the MSL vehicle. This remains an open question for future missions to consider.

In Fig. 20, the extracted axial force coefficient history in the low supersonic regime is plotted versus time compared to the preflight predicted values and best fit data, highlighting the departure. Also in this figure, one will notice a discrete jump in the MEADS C_A curve at the start of SUFR. At this point in the trajectory, both an entry balance mass is jettisoned and controller commands the EV to bank 180 deg. Further analysis identified the thrust contributions of the reaction control system to corrupt the accelerometer history used to extract C_A. As SUFR starts, the RCS jets (four and briefly six of the eight jets) fire to perform a 180 deg bank to put the capsule in a favorable position for the landing radar. Halfway through the maneuver, a reverse torque using the other four jets is commanded to arrest the bank rate. During much of this segment of the trajectory, four or six jets are firing at any given time and cycling rapidly. Each jet is commanded at eight Hertz with a prescribed duration of some fraction of the total duration between commands. This pulse-width modulation permits fine control of applied RCS moments. During SUFR, the duty cycles of the jets, when commanded, were roughly 50%, some peaking briefly near 100%. The only information available to attempt to correct for or remove the RCS thrust contribution from the DIMU accelerometer history was this RCS command history recorded during flight. It is likely that a time-accurate model of each RCS thrust (tied to the vehicle timeline), as well as the plume interactions with the wake, would be required for any meaningful correction. However, the DIMU accelerometer data were filtered to extract the aerodynamic coefficients. In attempting to correct for the RCS firings, it was found that the corrections were sensitive to the type of filter used. The variations were on the order of the corrections themselves. Although the contribution of filter error is well within the overall accuracy of the aerodynamic coefficient measurements, it presents a significant problem for any RCS correction. In the end, an RCS correction was deemed to be beyond the scope of this paper. However, an approximate C_A correction built using the duty cycle histories and the preflight thrust model of the RCS jets would tend to increase the measured C_A, thus mitigating the observed step at the start of SUFR. The authors are reasonably confident that the RCS thrust is the primary source of the C_A step at SUFR start. Reconstruction of any future mission with active RCS control should consider the interplay of RCS thrust, wake interactions, DIMU measurements, and data filtering when RCS thrusts are a significant fraction of the aerodynamic forces.

Again, it should be noted that these data are outside the dynamic pressure range of the MEADS experiment. The data are noisier in this low supersonic regime, but the data suggest that the vehicle saw a larger axial force coefficient than predicted. With no backshell pressure measurements, and forebody pressures limited to seven locations on the forebody, there can be no definitive determination that these anomalous measurements indicate a true deviation from the preflight predictions or are due to the instrumentation accuracy. These discrepancies are within the MEADS uncertainties (which increase rapidly below 850 Pa dynamic pressure) and, overall, preflight and MEADS data are in good agreement. It is not recommended that the Viking base correction be revisited, but backshell pressure instrumentation on future Mars entry vehicles

could help to better understand and quantify the total axial force acting on the vehicle in the supersonic region of the trajectory.

2. Transverse Force Coefficients

The MEADS-reconstructed normal force value and a comparison with the preflight aerodynamic database predictions are plotted in Fig. 21. The difference between the measured coefficient history and the prediction and best-fit dispersions (Fig. 21b) were calculated again using the aerodynamic database queried at the DIMU reconstructed attitude. Here, the absolute difference is plotted because the C_N dispersion included both an adder and a multiplier. The MEADS data are differenced with the C_N data scaled by the best-fit multiplier (a small correction). The best-fit C_N adder is also shown. Again, over most of the trajectory, the disagreement between flight data and prediction is captured with a constant adder well within the 3σ bounds. The magnitude of the normal force coefficient was slightly greater than predicted. Together, the small differences in normal and axial force coefficients counter each other to some extent, resulting in the good lift-to-drag agreement shown earlier.

There are several local discrepancies along the reconstructed C_N history. These are due to accelerations produced by RCS thrust during bank reversals. The corruption of the jet-off data is magnified as dynamic pressure decreases and the fixed thrust jets produce accelerations that become a larger fraction of those caused by aerodynamic forces. Near peak dynamic pressure, the RCS accelerations are barely discernible. It was mentioned for the C_A data that RCS thrust corrupted the measurements during SUFR. The RCS jets fired during bank reversals at high dynamic pressure produced little or no influence on the C_A measurements because the axial aerodynamic forces were much higher than the RCS thrusts (and normal and side forces).

Only the side force coefficient error is plotted in Fig. 22 because the nominal preflight prediction of C_Y is essentially zero. The side force remains close to zero over most of the trajectory, as predicted. This is primarily an indicator that the sideslip angle remained close to zero as discussed earlier. The noticeable deviations are again attributable to RCS firings during bank reversals. The magnitude of the RCS noise during bank reversals increases as dynamic pressure drops. Overall there is excellent agreement between preflight prediction and the normal and side force MEADS aerodynamic coefficients.

3. Static Stability

A comparison of the reconstructed static stability coefficients with those predicted by the aerodynamic database are shown in Fig. 23. An example of the fit of the body rate models, Eqs. (13) and (18), to the DIMU measured rates is shown in Fig. 23b. These fits are across one of the eight identified RCS-quiet segments along the trajectory and are representative of the others. The frequencies used to extract the static stability coefficient were obtained from the best fit of the model to the raw rate data. Notice the raw rate data is changing amplitude slightly, due to dynamic damping and changes in dynamic pressure, but over the course of one or two cycles, this effect is small and the fit of the constant amplitude sinusoid is quite good. There is excellent agreement between the extracted static stability coefficients and the predicted values. The greatest discrepancy of any point is approximately 5% between the predicted and reconstructed yaw stability at low supersonic speeds, which is small compared with the database static stability multiplier of 20%. Large gaps exist between data points in the hypersonic regime as the capsule performed numerous bank reversals. Therefore, stability derivatives near peak dynamic pressure conditions (Mach 18–20) could not be identified by this analysis, although the preflight predictions show almost constant stability coefficient values across this regime. The TF frequency analysis mentioned earlier indicated no anomalous variation in the static stability, although the results of that analysis were error prone, especially where dynamic pressure was changing rapidly. A more definitive comparison would require a period of RCS inactivity in that region.
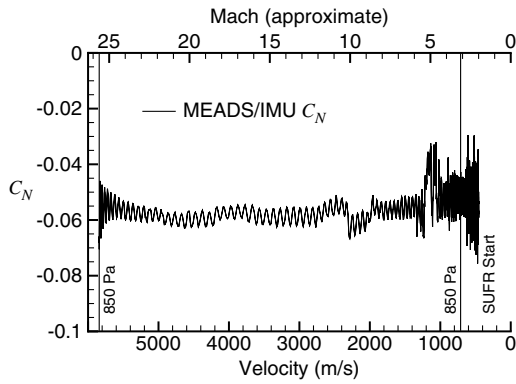
a) MEADS normal force coefficient

$$C_{N,\text{MEADS}} - (C_{N,\text{ADB}})(1+U_{C_N}^M)$$

$$U_{C_N}^A(1+U_{C_N}^M) \text{ fit}$$
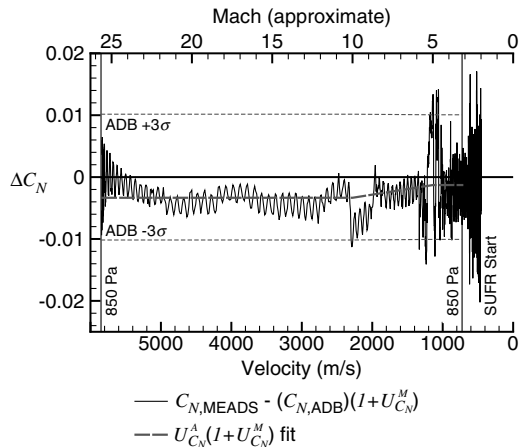
b) Prediction/reconstruction difference

Fig. 21   Reconstructed C_N and comparison with aerodynamic database C_N (called at DIMU α).

4. Best-Fit Dispersions

Table 2 lists the aerodynamic database dispersions identified by least-squares fit through the MEADS reconstructed coefficients. The "Fit to DIMU" column represents the adder and multiplier dispersions that best reconcile the aerodynamic database with the MEADS coefficients using the DIMU angle-of-attack history. For the force coefficient errors, these fits used only the data within the MEADS 850 Pa boundary, and so the large C_A divergence does not skew the supersonic fit. The force coefficient dispersions were used to plot the best-fit difference curves shown previously.

As described earlier, the uncertainties that best reconcile the database with flight data for the moment coefficients do not come from comparisons of the moment coefficients themselves. Rather, the adders that best reconciled the trim angles of attack and sideslip

(DIMU angle of attack and aerodynamic database for sideslip) were identified. The multipliers that best reconciled the static stability based on the DIMU body rates were identified as well.

Looking back at the comparison plots in this paper, it is remarkable that each coefficient can be brought into good agreement across most of the trajectory with only the two sets of dispersions used in the aerodynamic database for the two continuum flow flight regimes. Extracting uncertainties that vary along the entire trajectory would provide little additional information. For almost all of the variables, the identified dispersions show that the coefficients extracted from flight data are in agreement with predictions to within 1σ or better. It should be noted that the yawing moment adders, derived from a fit of the database to the accelerometer-based reconstruction of sideslip, do not reflect all the errors observed in the MEADS and DIMU reconstructions. The yaw adder dispersions are determined by the symmetry of the y accelerometer signal, which indicated a small sideslip angle. The case was made early as to why the MEADS transducer hysteresis effects and crosswinds affecting the MEADS and DIMU reconstructions produced erroneous sideslip measurements, but the true attitude of the vehicle may have been at greater sideslip than the accelerometers measured. The weighting of accelerometer error, wind effects, MEADS transducer hysteresis, and other effects cannot be separated definitively. The reconstructed uncertainties reflect the engineering judgment used in selecting the best reconstructed capsule state from the available data.

C. Interpretation of RCS Firing History

Some aerodynamic performance parameters could not be extracted explicitly. These include the dynamic stability characteristics, any persistent aerodynamic roll moments, and aerodynamic interactions with the reaction control system jet plumes. For each of these items, a qualitative assessment can be made based on comparisons of the RCS firing history to preflight predictions. Although not conclusive, this assessment is based on the interpretation of flight data with the
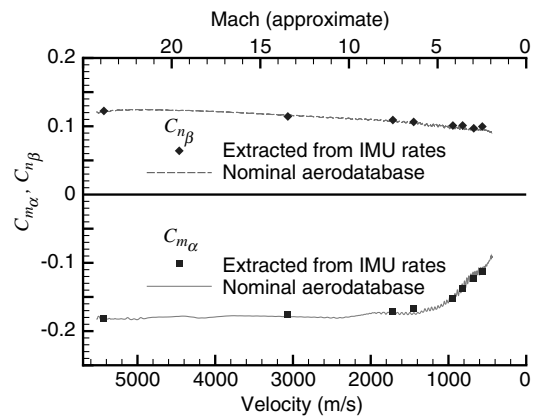
a) Stability coefficients
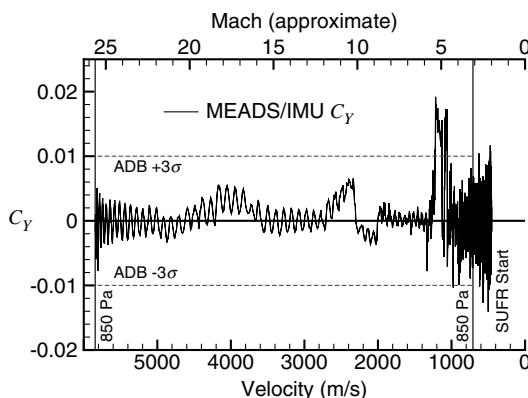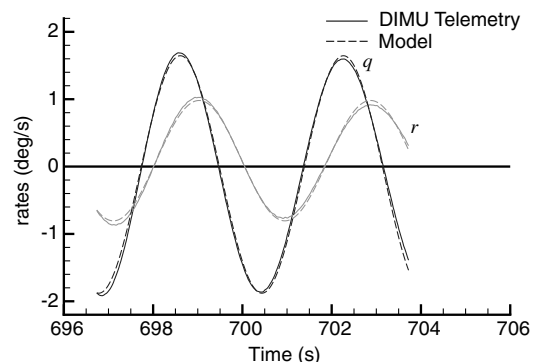

b) Fit of modeled rates (mach 3.6)

Fig. 23   Comparison of pitch and yaw static stability extracted from flight body rates with those predicted by MSL aerodynamic database.

Fig. 22   Reconstructed side force coefficient C_Y.

experience of sifting through many preflight predictions over the course of the MSL EDL development.

1. Aerodynamic Interactions with RCS

A large effort was undertaken during the MSL EV development to design and quantify the likely interactions of the RCS plumes with the surrounding wake environment [24,25]. The final interaction model used in the simulation predicted that RCS interactions would be small [26]. Monte Carlo analyses using the MSL POST2 simulation also showed that RCS fuel usage was essentially invariant within the interaction bounds set for the aerodynamic database. Stress testing beyond the nominal dispersions was performed with Monte Carlo analysis. The increased dispersion cases indicated that, as interactions increased, fuel usage increased until the interactions exceeded the nominal RCS torques and created control reversals. At the control reversal point, fuel usage departs (increases many fold over the nominal) as the vehicle struggles or fails to perform the maneuvers prescribed by the controller. The flight data show very little RCS activity except for the large bank reversals, minimal thrusting to maintain the desired bank angle within prescribed deadbands, and perhaps to bank the vehicle into the prevailing crosswind as described earlier. There does not appear to be any excessive firing at the time of the bank reversals that would indicate the flight RCS torques differing from the design values significantly. Available data suggest that the RCS interaction decrements (or even small augmenting increments) to control authority were small.

2. Dynamic Stability

Schoenenberger et al. [27] describe the ballistic range testing conducted for the MSL EV and how the extracted pitch damping coefficient C_{m_q} was implemented into the flight aerodynamic database. Because of facility constraints, all MSL ballistic range testing was conducted with nonlifting models. The nonlifting pitch damping data were applied in a conservative manner in the MSL database, shifting the peak instability observed at $\alpha = 0$ deg to the predicted trim angle of attack. The unshifted nonlifting data indicated that the pitch damping coefficient would be dynamically stable at the MSL trim angle, but there were insufficient data to predict what damping the lifting vehicle would experience. The flight data hint that shifting the damping data was overly conservative. Looking at preflight simulations, small oscillations were observed to grow in the supersonic regime, exceeding pitch-rate deadband limits specified in the controller algorithm. Exceeding this limit prompted the RCS system to fire pitch jets to damp the oscillations. Looking at the flight rates and RCS history, the EV never exceeded the rate deadbands before parachute deploy. This suggests the natural dynamic damping was greater than modeled in the aerodynamic database. The capsule appeared to act more like what the nonlifting ballistic range data would predict. Because the angle oscillations are small and the damping moments are only small modifiers to the static moments, it is difficult to extract any pitch damping data explicitly. However, all available data suggest the RCS controller was not called upon to damp rates induced by any inherent instability.

3. Roll Torques

Schoenenberger et al. [11] showed how recession on the heat shield might lead to a pinwheel aerodynamic effect causing adverse roll moments. In off-nominal simulations, it was shown that severe roll torques near peak dynamic pressure could overpower RCS control authority during bank reversals, causing the vehicle to fall off the guided trajectory and miss the desired landing ellipse. The RCS firing history complicates the search for adverse roll moments. A quiescent segment of the trajectory is necessary to identify any natural aerodynamic rolling moment. The frequency of RCS firing interrupts the "quiet" glide of the MSL capsule. The longest segment of data near the peak dynamic pressure point indicates negligible off-nominal roll torque. One percent of the 3σ value listed in Table 1 is all that is required to replicate the minimal roll rate change over the quiescent segments. The minimal RCS firing activity away from the

Table 2   Table of dispersions reconciling aerodynamic database and MEADS aerocoefficients

Coefficient	Dispersion	Regime	3σ	Fit to DIMU	DIMU/3σ
C_A	U_{C_A}	Supersonic	10%	+3.28%	0.3282
		Hypersonic	3%	+1.08%	0.3600
C_N	$U^A_{C_N}$	Supersonic	0.01	−0.001274	−0.1274
		Hypersonic	0.01	−0.003285	−0.3285
	$U^M_{C_N}$	Supersonic	10%	0.698%	0.0698
		Hypersonic	10%	1.634%	0.1634
C_m	$U^A_{C_m}$	Supersonic	0.005	−0.00043	−0.0856
		Hypersonic	0.006	0.00046	0.0768
	$U^M_{C_m}$ [a]	Supersonic	20%	0.576%	0.0288
		Hypersonic	20%	−1.228%	−0.0614
C_n	$U^A_{C_n}$ [b]	Supersonic	0.005	0.000006	0.0004
		Hypersonic	0.003	−0.00001	−0.0041
	$U^M_{C_n}$ [a]	Supersonic	20%	3.386%	0.1693
		Hypersonic	20%	−0.1126%	−0.0056

[a]Determined by fit to body rates.
[b]Determined by fit to ADB history.

necessary bank reversals also suggests the controller was not fighting any anomalous aerodynamic moments.

IV.   Conclusions

The reconstructed Mars Science Laboratory entry capsule aerodynamic coefficients compare remarkably well with preflight predictions. The trim angle of attack was predicted accurately and the reconstructed lift-to-drag ratio exceeded predictions by only a small percentage for most of the entry. Reconciliation of the MSL aerodynamic database with MEADS/accelerometer aerodynamic coefficients showed that the force coefficient dispersions were in agreement with flight data to about 1σ or better. Reconciliation of the moment dispersions by fits to the trim angle and body rate data yielded similar agreement. It is notable how well the data are reconciled across the entire entry using only the few uncertainty parameters in the MSL aerodynamic database.

Two small anomalies have been identified in the reconstruction process. First, the axial force coefficient extracted from the MEADS dynamic pressure and the DIMU axial accelerometer is much greater than preflight predictions in the supersonic regime leading up to balance mass jettison. This may be due to instrumentation error, reconstruction error, or the aerodynamic database base pressure correction. The data suggest that it is some kind of instrumentation error, which is not unreasonable because this segment of the trajectory was outside the design space for the MEADS experiment. The other notable anomaly is the divergence in sideslip as the vehicle slows to supersonic speeds before the SUFR maneuver. Both MEADS and DIMU angle reconstructions show a similar divergence, but this appears to be due to two different sources of error. The DIMU accelerometers were used with the MSL aerodynamic database to reconstruct the sideslip angle semi-independent of the other methods. The accelerometer results indicate there was no sideslip divergence during entry. The MEADS angle measurement uncertainties are greater than the sideslip angle reconstructed with the pressure data and a review of calibration data shows that hysteresis loops are a characteristic of the flight transducers when put through a pressure pulse with a duration like the MSL entry. Variations in the hysteresis loops from transducer to transducer are on the order of 20–30 Pa. Such a difference between MEADS ports 6 and 7 is the likely explanation for the MEADS β divergence. The DIMU β divergence is consistent with the MSL entry vehicle flying a "crosswind landing" leading up to the SUFR maneuver and parachute deploy. To maintain the proper ground track, the vehicle banked into a north-to-south wind and the natural stability of the capsule resulted in a crab angle, which was measured as a sideslip angle in the DIMU reconstruction.

Overall preflight aerodynamic predictions were excellent. The MSL aerodynamic database accurately predicted the flight performance and a database of similar fidelity could be used again with no

improvements for a similar mission in the future. The RCS interactions and dynamic stability characteristics appeared to be benign with no obvious adverse effects on the flight performance. No unexpected roll torques were observed. Although the MSL aerodynamic database performed quite well, further analysis may be able to refine the nominal aerodynamic data model for future missions or may be able to justify reducing uncertainties to wring additional performance from the MSL EV. Better pressure instrumentation, especially in the low supersonic regime, could resolve the axial force anomaly and perhaps reduce β errors and more accurately measure the wind environment. Any pressure instrumentation improvements or augmentation should include the addition of pressure transducers on the aftbody to quantify its contribution to C_A. Aftbody pressure measurements could replace Viking-derived base corrections and possibly help improve CFD wake solutions. Sizing the forebody pressure transducer full-scale range for the low supersonic regime would improve the capsule attitude and C_A measurement accuracy and more accurately determine atmospheric winds. Resolving the disagreement between the predicted and reconstructed supersonic axial force coefficient and eliminating the remaining ambiguity in the sideslip measurements would improve the flight performance of future Mars entry vehicles and decrease landing ellipse size to a smaller size than the MSL landing area.

Acknowledgments

References

[1] Spencer, D. A., Blanchard, R. C., Braun, R. D., Kallemeyn, P. H., and Thurman, S. W., "Mars Pathfinder Entry, Descent, and Landing Reconstruction," *Journal of Spacecraft and Rockets*, Vol. 36, No. 3, May–June 1999, pp. 357–366.
doi:10.2514/2.3478

[2] Desai, P. N., Schoenenberger, M., and Cheatwood, F. M., "Mars Exploration Rover Six-Degree-of-Freedom Entry Trajectory Analysis," *Journal of Spacecraft and Rockets*, Vol. 43, No. 5, Sept.–Oct. 2006, pp. 1019–1025.
doi:10.2514/1.6008

[3] Desai, P. N., Prince, J. L., Queen, E. M., Schoenenberger, M., Cruz, J. R., and Grover, M. R., "Entry, Descent and Landing Performance of the Mars Phoenix Lander," *Journal of Spacecraft and Rockets*, Vol. 48, No. 5, Sept.–Oct. 2011, pp. 798–808.
doi:10.2514/1.48239

[4] Holmberg, N. A., and Faust, R. P., "Viking '75 Spacecraft Design and Test Summary, Volume 1—Lander Design," NASA RP-1027, Nov. 1980.

[5] Ingoldby, R. N., Michel, F. C., Flaherty, T. M., Doty, M. G., Preston, B., Villyard, K. W., and Steele, R. D., "Entry Data Analysis for Viking Landers 1 and 2," Martin Marietta Corp. TN-3770218, Denver, CO, Nov. 1976.

[6] Blanchard, R. C., and Walberg, G. D., "Determination of the Hypersonic/Rarefied-Flow Drag Coefficient of the Viking Lander Capsule 1 Aeroshell from Flight Data," NASA TP-1793, Dec. 1980.

[7] Flaherty, T. M., "Aerodynamics Data Book," Martin Marietta Corp. TR-3709014, Denver, CO, June 1972.

[8] Sell, S., "Powered Flight Design and Reconstructed Performance of the Mars Science Laboratory Mission," American Astronautical Society Paper 2013-0424, 2013.

[9] Cheatwood, F. M., and Gnoffo, P. A., "User's Manual for the Langley Aerothermodynamic Upwind Relaxation Algorithm (LAURA)," NASA TM-4674, 1996.

[10] Riley, C., and Cheatwood, F., "Distributed-Memory Computing with the Langley Aerothermodynamic Upwind Relaxation Algorithm (LAURA)," *Advances in Engineering Software*, Vol. 29, Nos. 3–6, July 1998, pp. 317–324.
doi:10.1016/S0965-9978(97)00074-4

[11] Schoenenberger, M., Dyakonov, A., Buning, P., Scallion, W., and Van Norman, J., "Aerodynamic Challenges for the Mars Science Laboratory Entry, Descent and Landing," AIAA Paper 2009-3914, 2009.

[12] Dyakonov, A. A., Schoenenberger, M., and Van Norman, J. W., "Hypersonic and Supersonic Static Aerodynamics of Mars Science Laboratory Entry Vehicle," AIAA Paper 2012-2999, 2012.

[13] Karlgaard, C. D., Tartabini, P. V., Blanchard, R. C., Kirsch, M., and Toniolo, M. D., "Hyper-X Post-Flight Trajectory Reconstruction," *Journal of Spacecraft and Rockets*, Vol. 43, No. 1, 2006, pp. 105–115.
doi:10.2514/1.12733

[14] Karlgaard, C. D., Beck, R. E., Derry, S. D., Brandon, J. M., Starr, B. R., Tartabini, P. V., and Olds, A. D., "Ares 1-X Trajectory Reconstruction: Methodology and Results," *Journal of Spacecraft and Rockets*, Vol. 50, No. 3, 2013, pp. 641–661.
doi:10.2514/1.A32345

[15] Karlgaard, C. D., Beck, R. E., O'Keefe, S. A., Siemers, P. M., White, B. A., Engelund, W. C., and Munk, M. M., "Mars Entry Atmospheric Data System Modeling and Algorithm Development," AIAA Paper 2009-3916, 2009.

[16] Munk, M. M., Little, A., Kuhl, C., Bose, D., and Santos, J., "Mars Science Laboratory (MSL) Entry, Descent and Landing Instrumentation (MEDLI) Hardware," American Astronautical Society Paper 2013-0310, 2013.

[17] Karlgaard, C. D., Kutty, P., Shidner, J., Schoenenberger, M., and Munk, M. M., "Mars Entry Atmospheric Data System Trajectory Reconstruction Algorithms and Flight Results," AIAA Paper 2013-0028, 2013.

[18] Karlgaard, C. D., Schoenenberger, M., Kutty, P., and Shidner, J., "Mars Science Laboratory Entry, Descent and Landing Trajectory and Atmosphere Reconstruction," American Astronautical Society Paper 2013-0307, 2013.

[19] Karlgaard, C. D., Kutty, P., Schoenenberger, M., Munk, M. M., Little, A., Kuhl, C., and Shidner, J., "Mars Entry Atmospheric Data System Trajectory and Atmosphere Reconstruction of the Mars Science Laboratory Entry, Descent and Landing," *Journal of Spacecraft and Rockets* (accepted for publication).

[20] Brauer, G. L., Cornick, D. E., and Stevenson, R., "Capabilities and Applications of the Program to Optimize Simulated Trajectories (POST)," NASA CR-2770, Feb. 1977.

[21] Gordon, S., and McBride, B. J., "Computer Program for Calculation of Complex Chemical Equilibrium Compositions and Applications," NASA RP-1311, 1994.

[22] Schoenenberger, M., Queen, E., Kutty, P., and Karlgaard, C., "Aerodynamics of Axisymmetric Blunt Bodies Flying at Angle of Attack," *IEEE Aerospace Conference*, Big Sky, Montana, Paper 2283, March 2014.

[23] Auger, F., and Flandrin, P., "Improving the Readability of Time-Frequency and Time-Scale Representations by the Reassignment Method," *IEEE Transactions on Signal Processing*, Vol. 43, No. 5, 1995, pp. 1068–1089.
doi:10.1109/78.382394

[24] Dyakonov, A. A., , Glass, C. E., Edquist, K. T., Schoenenberger, M., Chwalowski, P., Van Norman, J., Scallion, W. I., Tang, C., Wright, M. J., and Cheatwood, F. M. et al., "Design Considerations for Reaction Control Systems," *Fifth International Planetary Probe Workshop*, June 2007, http://solarsystem.nasa.gov/missions/ippw05_sessions.cfm#session06.

[25] Dyakonov, A. A., Schoenenberger, M., Scallion, W. I., Van Norman, J., Novak, L., and Tang, C., "Aerodynamic Interference Due to MSL Reaction Control System," AIAA Paper 2009-3915, 2009.

[26] Schoenenberger, M., Van Norman, J., Rhode, M., and Paulson, J., "Characterization of Aerodynamic Interactions with the Mars Science Laboratory Reaction Control System Using Computation and Experiment," AIAA Paper 2013-0971, 2013.

[27] Schoenenberger, M., Yates, L., and Hathaway, W., "Dynamic Stability Testing of the Mars Science Laboratory Entry Capsule," AIAA Paper 2009-3917, 2009.

R. Braun
Associate Editor